JACS
JOURNAL OF THE AMERICAN CHEMICAL SOCIETY
Article
Cite This: J. Am. Chem. Soc. 2019, 141, 8928−8936
pubs.acs.org/JACS

Defect-Mediated Phase Transformation in Anisotropic Two-Dimensional $PdSe_2$ Crystals for Seamless Electrical Contacts

Akinola D. Oyedele,[†,‡,#] Shize Yang,[§,#] Tianli Feng,[§,∥,#] Amanda V. Haglund,[‡,⊥] Yiyi Gu,[†,▲] Alexander A. Puretzky,[†] Dayrl Briggs,[†] Christopher M. Rouleau,[†] Matthew F. Chisholm,[§] Raymond R. Unocic,[†] David Mandrus,[§,⊥] Harry M. Meyer, III,[†] Sokrates T. Pantelides,[§,∥] David B. Geohegan,[†] and Kai Xiao*[,†,‡]

[†]Center for Nanophase Materials Sciences and [§]Materials Science and Technology Division, Oak Ridge National Laboratory, Oak Ridge, Tennessee 37830, United States

[‡]Bredesen Center for Interdisciplinary and Graduate Education and [⊥]Department of Materials Science and Engineering, University of Tennessee, Knoxville, Tennessee 37996, United States

[∥]Department of Physics and Astronomy and Department of Electrical Engineering and Computer Science, Vanderbilt University, Nashville, Tennessee 37235, United States

[▲]Key Laboratory of Photochemical Conversion and Optoelectronic Materials, Technical Institute of Physics and Chemistry, Chinese Academy of Sciences, Beijing 100190, P.R. China

Supporting Information

ABSTRACT: The failure to achieve stable Ohmic contacts in two-dimensional material devices currently limits their promised performance and integration. Here we demonstrate that a phase transformation in a region of a layered semiconductor, $PdSe_2$, can form a contiguous metallic $Pd_{17}Se_{15}$ phase, leading to the formation of seamless Ohmic contacts for field-effect transistors. This phase transition is driven by defects created by exposure to an argon plasma. Cross-sectional scanning transmission electron microscopy is combined with theoretical calculations to elucidate how plasma-induced Se vacancies mediate the phase transformation. The resulting $Pd_{17}Se_{15}$ phase is stable and shares the same native chemical bonds with the original $PdSe_2$ phase, thereby forming an atomically sharp $Pd_{17}Se_{15}/PdSe_2$ interface. These $Pd_{17}Se_{15}$ contacts exhibit a low contact resistance of ∼0.75 kΩ μm and Schottky barrier height of ∼3.3 meV, enabling nearly a 20-fold increase of carrier mobility in $PdSe_2$ transistors compared to that of traditional Ti/Au contacts. This finding opens new possibilities in the development of better electrical contacts for practical applications of 2D materials.

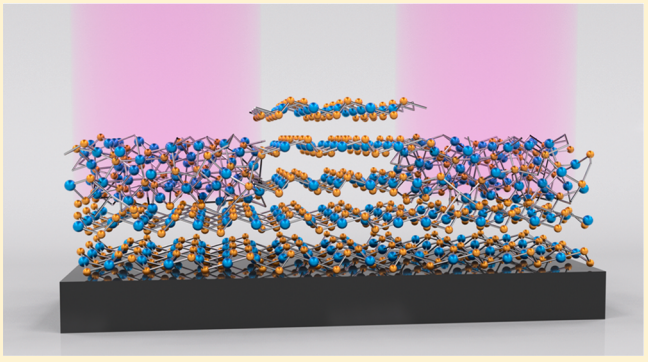

INTRODUCTION

One of the key challenges limiting the integration and performance of semiconducting two-dimensional (2D) materials for next-generation electronic devices is the high resistance of contacts with traditional metal electrodes.[1,2] Despite careful selection of metals to adjust the band alignment for reduced tunnel barriers at metal/2D-semiconductor interfaces,[3] often metal/2D-semiconductor alloys or metal-induced gap states are formed that lead to Fermi-level pinning and a large and unstable Schottky barrier (SB).[4,5] The use of metallic 2D materials, such as graphene or metallic transition-metal dichalcogenides (TMDs), as contacts to obviate these problems,[6−8] is one approach that has been shown to significantly reduce the contact resistance, but the transfer process required to fabricate these contacts is not well-controlled at present.[9,10]

An alternate and highly promising approach to solve the contact resistance problem is through the synthesis of chemically bonded heterojunctions between metallic and semiconducting regions of 2D materials to form seamless contacts.[2] This objective is most elegantly accomplished through phase engineering a 2D crystal by a variety of top-down processing approaches. For example, such seamless contacts have recently been demonstrated by converting regions of semiconducting *2H*-MoS_2 to metallic *1T*-MoS_2 phase through selective chemical doping, yielding a low contact resistance of 0.2 kΩ μm.[11] A variety of other processing methods to phase engineer 2D materials to induce metallic phases are also being explored, including laser/plasma/electron/ion beam irradiations,[12−16] electrostatic dop-

Received: March 8, 2019
Published: May 15, 2019

DOI: 10.1021/jacs.9b02593
J. Am. Chem. Soc. 2019, 141, 8928−8936

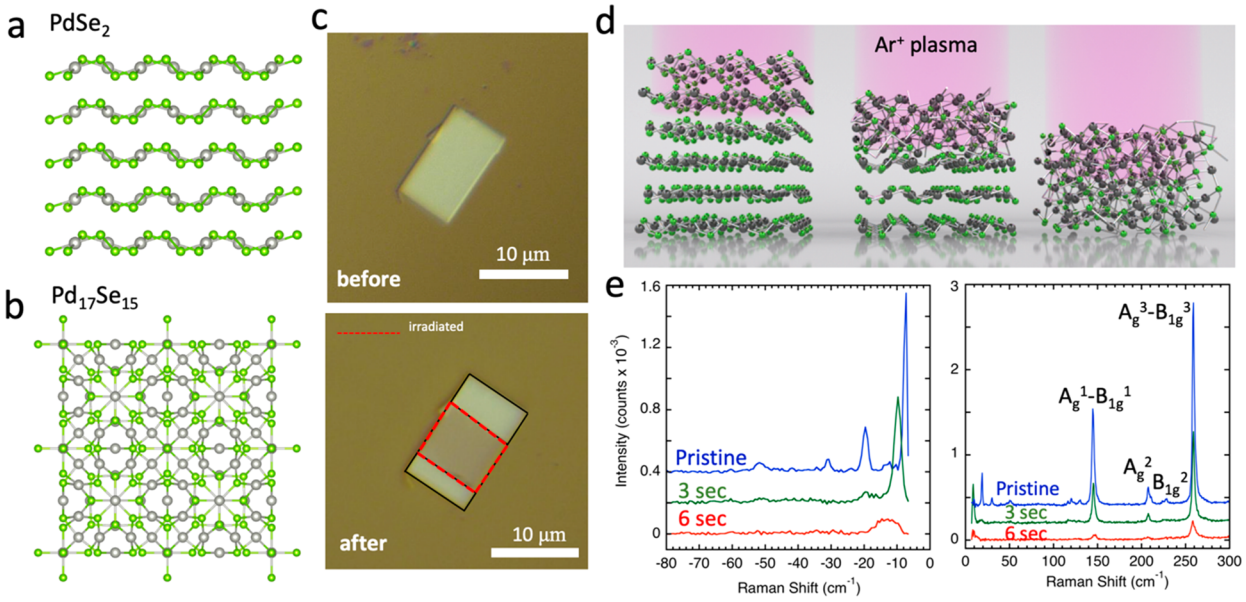

Figure 1. Structure and plasma-irradiation processing of 2D $PdSe_2$. Lattice structures (a) $PdSe_2$ and (b) $Pd_{17}Se_{15}$. Green spheres are Se atoms and gray spheres are Pd atoms. (c) Optical images of a thick $PdSe_2$ flake before and after 10 s argon-plasma treatment. The irradiated area is highlighted by the red dashes. (d) Schematic diagram illustrating the plasma-treatment process. (e) Raman spectroscopy of a pristine $PdSe_2$ flake and after irradiation with different times. (left) Anti-Stokes low-frequency (LF) Raman spectra.

ing,[17] metal intercalation,[18] and polymorphic epitaxy.[19] However, the failure to realize a stable metallic phase with thermal and air stability has limited their technological value for practical electronics.

Palladium diselenide ($PdSe_2$) is a recently discovered layered 2D semiconductor that has high stability under ambient conditions, and high electron mobility.[20,21] The layer-number-dependent band gap in $PdSe_2$, which varies from 0 eV (bulk) to 1.3 eV (monolayer), is appealing for tunable 2D optoelectronic applications.[20] Unlike most 2D materials, $PdSe_2$ exhibits pentagonal bonding and a unique anisotropic structure with unusual 4-fold coordination of the metal atoms and intralayer bonding between the chalcogen atoms. As a result, its layers are puckered and strongly interacting, making it an interesting candidate for phase engineering. By weakening of Se−Se intralayer bonds under high pressure, the layered $PdSe_2$ orthorhombic phase can be transformed into various polymorphic phases that include the following: a layered monoclinic phase,[22] a layered 1T phase[23,24] (which has been shown in other group-10 TMDs to exhibit Dirac semimetallic and superconducting properties[25,26]), or a pyrite-type phase (exhibiting superconductivity below T_c = 13.1 K and theoretically predicted topological states[27]). In addition, by alteration of the stoichiometry of palladium selenide compounds, a wide range of binary phases can be accessed to provide an extra degree of freedom for phase engineering.[28] For example, $Pd_{17}Se_{15}$, Pd_7Se_4, and Pd_4Se have nonlayered structures that exhibit metallic and superconducting behavior confirmed experimentally[15,28−30] and topological quantum properties predicted theoretically.[31] Therefore, the highly anisotropic structure of $PdSe_2$ coupled with the variety of known $PdSe_2$ polymorphs and Pd−Se binary phases offers enormous opportunities to exploit local phase transitions for the creation of stable heterophase structures to utilize as seamless Ohmic contacts for 2D devices. A variety of processing methods may be promising to induce such phase transitions, including laser irradiation,[7] electrical field,[32] ion/electron-beam irradiation,[15,33] or strain.[27,34] However, unlike isotropic 2D materials,[12,14,35] understanding the mechanisms of phase transformations in $PdSe_2$ is complicated by its highly anisotropic structure.

In this article, we report the experimental demonstration of a defect-driven phase transformation by plasma irradiation in few-layered $PdSe_2$ crystals. The metallic $Pd_{17}Se_{15}$ phase, which exists naturally and is known as palladesite,[22] is obtained from layered $PdSe_2$ under Ar-plasma irradiation and is clearly identified by atomic resolution scanning transmission electron microscopy (STEM). Using cross-sectional STEM imaging and DFT calculations, we describe the transformation process with atomic-scale detail and demonstrate that the Ar-plasma-induced Se vacancies within the highly anisotropic $PdSe_2$ initiate the phase transformation from layered $PdSe_2$ to non layered $Pd_{17}Se_{15}$. With selective plasma irradiation, hetero-phase $Pd_{17}Se_{15}/PdSe_2$ junctions with atomically sharp interfaces are fabricated. Such junctions provide seamless Ohmic contacts for $PdSe_2$ transistors and substantially improved device performance compared to that of common Ti/Au contacts.

RESULTS AND DISCUSSION

Bulk $PdSe_2$ single crystals were synthesized by a self-flux method as previously reported.[20] The lattice structures of $PdSe_2$ and $Pd_{17}Se_{15}$ are schematically shown in Figure 1(a) and (b), respectively. $PdSe_2$ has a unique pentagonal network with a puckered lattice structure in which each layer is a Se−Pd−Se trilayer with a tilted Se−Se dumbbell crossing the Pd layer. Such structure lacks rotational symmetry, making it very sensitive to defects, especially Se vacancies.[15,32] In contrast, $Pd_{17}Se_{15}$ is a naturally existing mineral with stable cubic structure that has short Pd−Pd bonds exhibiting cagelike nonlayered structures.[22] Strong Pd−Pd interactions in $Pd_{17}Se_{15}$ lead to a narrow 4d band at the Fermi level, resulting in a superconducting phase at 2.2 K.[30]

DOI: 10.1021/jacs.9b02593
J. Am. Chem. Soc. 2019, 141, 8928−8936

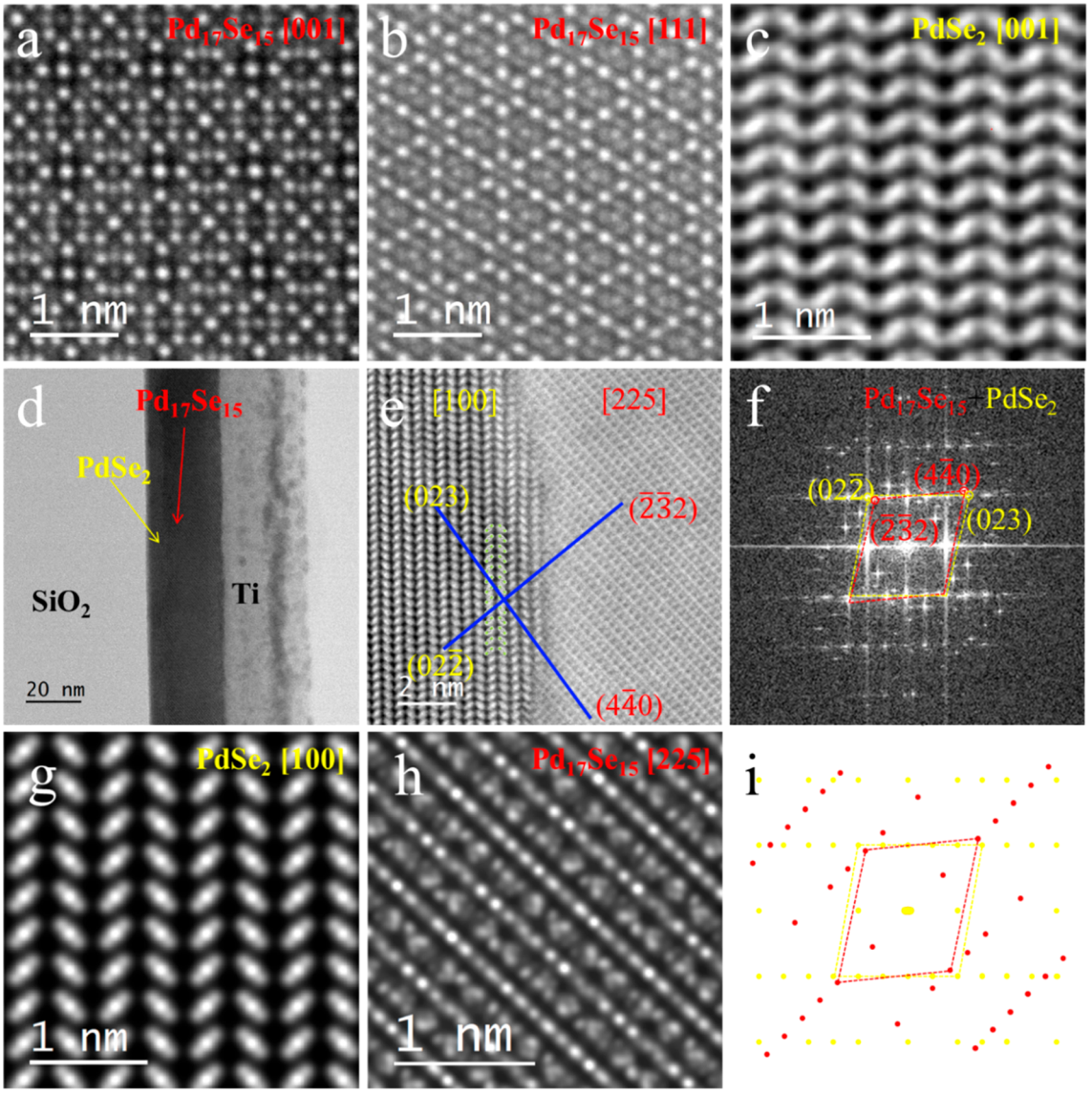

Figure 2. STEM characterizations of crystal structure of $Pd_{17}Se_{15}$ and its interface with $PdSe_2$. ADF-STEM images of $Pd_{17}Se_{15}$ viewed along [001] zone axis (a) and along [111] zone axis (b) are shown. (c) Experimental ADF image of pristine $PdSe_2$. (d) A low-magnification cross-sectional bright-field STEM image of the interface region between $PdSe_2$ and $Pd_{17}Se_{15}$. A high-magnification cross-sectional ADF-STEM image in (e) shows that the interface between the (001) plane of $PdSe_2$ and $(0\bar{3}1)$ plane of $Pd_{17}Se_{15}$ is atomically sharp. Image simulations of $PdSe_2$ (g) and $Pd_{17}Se_{15}$ (h) phases in (e) are also provided, which agree with experiment very well. ADF-STEM FFT patterns (f) taken from the $Pd_{17}Se_{15}/PdSe_2$ interface region in (e). The diffraction spots labeled with yellow color and red color are from $PdSe_2$ region and $Pd_{17}Se_{15}$ region, respectively. The simulated diffraction patterns are shown in (i).

Plasma treatment is a scalable and industry-compatible method that has been used to create defects,[36] decrease the number of layers,[37] and induce phase transitions in 2D materials.[13,35] Here, few-layer $PdSe_2$ was mechanically exfoliated from bulk crystals and then placed on a Si/SiO_2 substrate with a 20-nm-thick SiO_2 layer as shown in Figure 1c. The sample was subsequently treated by Ar plasma that resulted in the $PdSe_2$ phase transformation, which was strongly dependent on both the radio frequency (RF) power used to generate the Ar plasma and on the $PdSe_2$ treatment time (see details in the Experimental Section and Figure S1, Supporting Information). A schematic illustration of the phase transformation in 2D $PdSe_2$ flakes by plasma treatment is shown in Figure 1d. Ar-plasma treatment of the central area of a rectangular $PdSe_2$ crystal decreases the observed optical contrast of the treated area (Figure 1c), indicating a decrease in the number of layers.

To understand the evolution of $PdSe_2$ to $Pd_{17}Se_{15}$, we conducted Raman measurements on pristine $PdSe_2$ crystals before and after Ar-plasma treatment using different plasma exposure times. The pristine $PdSe_2$ crystals exhibit three distinct A_g and B_{1g} high-frequency (HF) Raman modes near 145, 208, and 260 cm^{-1} as well as the low-frequency (LF) breathing modes (Figure 1e (right panel)) that depend strongly on the number of layers and provide fingerprints for thickness determination.[2,20,38] For example, the LF Raman spectrum of a pristine $PdSe_2$ crystal shown in Figure 1e (left panel) exhibits peaks at 7, 20, 31, 42, and ~52 cm^{-1} that match well with the 13 branches of the breathing mode at B1 (7 cm^{-1}), B3 (20 cm^{-1}), B5 (30 cm^{-1}), B7 (40 cm^{-1}), B11 (50 cm^{-1}), and B13 (52 cm^{-1}) corresponding to a 15 layer crystal

DOI: 10.1021/jacs.9b02593
J. Am. Chem. Soc. 2019, 141, 8928−8936

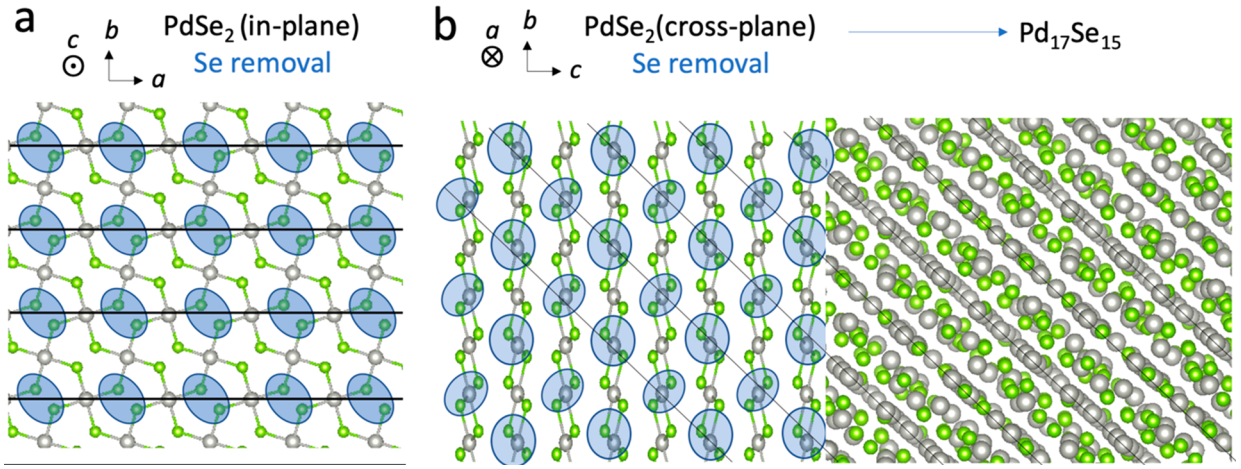

Figure 3. Transformation pathway from layered $PdSe_2$ to cubic $Pd_{17}Se_{15}$. The Se atoms in blue-shaded areas are preferentially removed by Ar ions. (a) Se vacancies formed in a single layer; (b) Se vacancies formed across the layers under plasma irradiation.

(~7 nm) on the basis of our previous studies.[38] After the plasma treatment, the peak positions of the HF modes do not change significantly. However, the B1 (7 cm^{-1}) LF Raman peak shifts to ~10 cm^{-1} after 3 s of plasma treatment, corresponding to 10−11 layers. In addition, this spectrum does not show pronounced higher branches of the breathing mode, which indicates that the reduced layers are defective. After 6 s of plasma irradiation, the breathing mode almost disappears (Figure 1e; see also Figure S2 and Table S1). These Raman measurements clearly show that thinning of $PdSe_2$ crystals and creation of defects occur after a relatively short plasma treatment. The longer plasma irradiation with the same RF power eliminates the LF-Raman modes and leaves the HF modes approximately at the same positions, possibly indicating a phase transition in $PdSe_2$.

The chemical composition of the plasma-irradiated $PdSe_2$ flakes was investigated by Nano-Auger electron spectroscopy (NAES). Auger mapping clearly shows that the Se/Pd ratio at the plasma-irradiated region changes to 0.9, which is consistent with the stoichiometry of $Pd_{17}Se_{15}$. The NAES line profile measured across the $PdSe_2$−$Pd_{17}Se_{15}$ junction demonstrates that appearance of the new phase is associated with Se loss from the layered $PdSe_2$ structure (see Figure S3 in the Supporting Information for details).

The atomic structures of the pristine and irradiated regions as well as their heterophase boundaries were studied by STEM. As shown in Figure 2a,b, the STEM annular dark-field (ADF) images of the [001] and [111] projections of the phase formed by plasma irradiation show a transformed surface region with a totally different structure from that of pristine $PdSe_2$ seen in Figure 2c. The experimental lattice parameter of the new phase was determined to be a = 11.2 Å. The hexagonal symmetry and 4-fold symmetry from the [111] and [001] projections clearly confirm the high-symmetry structure of $Pd_{17}Se_{15}$. Image simulations based on the known structure of $Pd_{17}Se_{15}$ (Figure S4) agree well with experimental images. With control of the etching time, the $PdSe_2$ can be partially converted to the $Pd_{17}Se_{15}$ phase. A low-magnification bright-field image in Figure 2d shows the cross-sectional interface between (~6.8 nm) $PdSe_2$ and (~20 nm) $Pd_{17}Se_{15}$ clearly. An enlarged ADF image (Figure 2e) shows an atomically sharp interface plane between the (001) surface of $PdSe_2$ and the $(0\bar{3}1)$ surface of $Pd_{17}Se_{15}$, which are verified by the FFT image of Figure 2f. The experimental images in Figure 2e agree well with simulated ADF images as shown in Figure 2g,h. Images of the $Pd_{17}Se_{15}$ phase along its [225] zone axis show that the (023) and $(02\bar{2})$ planes in $PdSe_2$ phase are aligned with the $(\bar{4}40)$ and $(\bar{2}\,\bar{3}2)$ planes in $Pd_{17}Se_{15}$. We have simulated the electron diffraction patterns as shown in Figure 2i which match the FFT of the experimental images of Figure 2f. As shown in Figure S6, the Pd site intensity in $PdSe_2$ is nearly the same across different positions close to the interface. However, the Se site intensities vary considerably, which can be explained by the formation of Se vacancies near the interface region during plasma treatment. These Se vacancies can lower the diffusion barrier and facilitate the phase transformation. Note that, on the basis of our observations, the phase transformation from $PdSe_2$ to $Pd_{17}Se_{15}$ is an irreversible process and the resultant phase is very stable but changes to polycrystalline under electron beam irradiation (Figure S7). In addition, we found that further exposure to Ar plasma only leads to $Pd_{17}Se_{15}$ thickness reduction without other binary Pd−Se phases evolving because of the stability of the $Pd_{17}Se_{15}$. The relatively high energy of our plasma leads to loss of more than 50% of Se atoms, enabling the formation of vacancy pairs, which according to theory presented here, then mediate the transformation to $Pd_{17}Se_{15}$. This phase is one of the most stable phases of the Pd−Se system. Lower-energy irradiation is known to lead to the formation of Pd_2Se_3.[15] In principle, by tuning the plasma energy, one can control the nature of the generated defects and achieve other phases.

On the basis of the above experiments, we can propose the following phase transformation mechanism in $PdSe_2$. During Ar-plasma irradiation, the Ar^+ ions impinge on the surface of $PdSe_2$ and transfer enough kinetic energy to break the Pd−Se and Se−Se bonds, resulting in Se vacancies. Unlike in commonly observed layered TMDs, where the lattice is still retained even at a relatively high concentration of chalcogen vacancies,[39] the highly anisotropic structure of $PdSe_2$ with strong interlayer interaction makes it very sensitive to defects. The Se vacancies break the symmetry of the Se−Se dumbbell and induce large structural distortions. As previously reported, the Se vacancies can diffuse both vertically and laterally in $PdSe_2$ because of the unique anisotropic network with strong interlayer binding energy in $PdSe_2$ compared to MoS_2. Note that the energy barrier for the interlayer Se vacancy diffusion in $PdSe_2$ is 1.59 eV, compared to 4.44 eV for MoS_2.[15,32] During

DOI: 10.1021/jacs.9b02593
J. Am. Chem. Soc. 2019, 141, 8928−8936

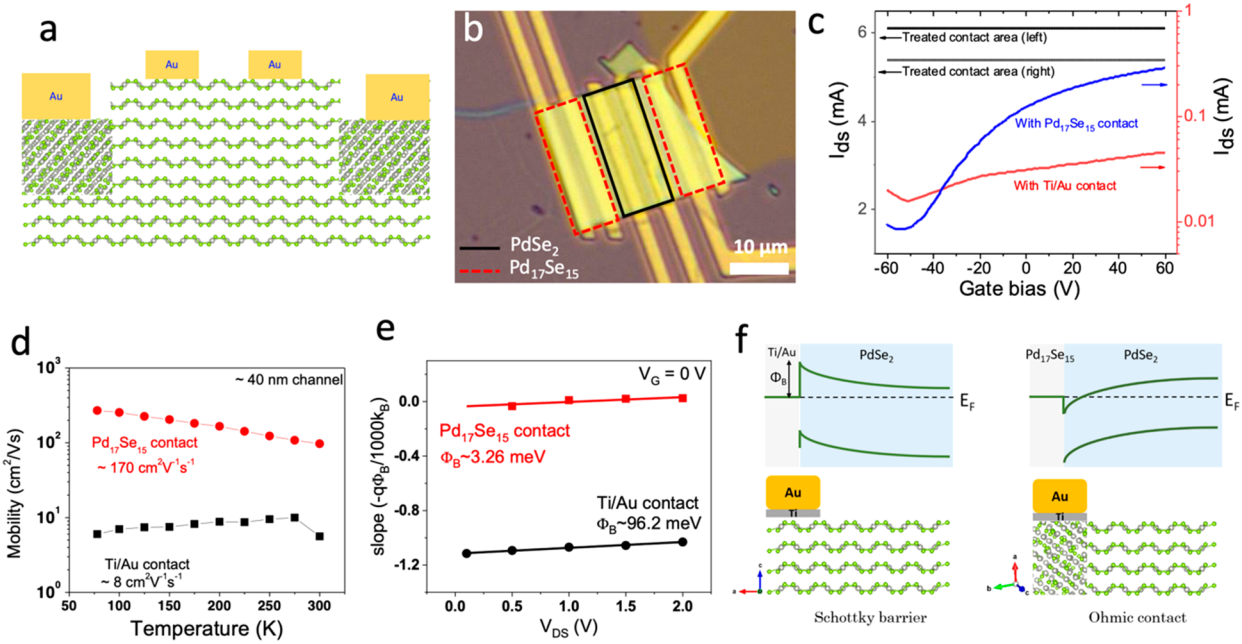

Figure 4. Electrical performances of $PdSe_2$ devices with $Pd_{17}Se_{15}$ contacts. (a) Schematic diagram of a device with a $PdSe_2/Pd_{17}Se_{15}$ phase heterojunction. (b) Optical image of a $PdSe_2$ device, with irradiated contact area used to obtain the transport properties of irradiated area, pristine channel with traditional Ti/Au contact, and pristine channel with $Pd_{17}Se_{15}$ contacts. The Ti/Au metal contact was carefully placed only on the $Pd_{17}Se_{15}$ phase without touching the edge of the $PdSe_2$ channel to eliminate the effect of the $PdSe_2$ and Ti/Au contact interface. (c) Transfer curves of the irradiated region, $PdSe_2$ channel with Ti/Au contact, and $PdSe_2$ channel with $Pd_{17}Se_{15}$ contact. (d) Field-effect mobility comparison as a function of temperature for thick $PdSe_2$ channels with Ti/Au and $Pd_{17}Se_{15}$ metal contacts. (e) Comparison of the Schottky barrier heights at the Ti/Au/$PdSe_2$ and $Pd_{17}Se_{15}$/$PdSe_2$ interfaces. (f) Schematic diagram illustrating Schottky (left) and Ohmic (right) contacts.

plasma treatment, new Se vacancies are continuously produced. With increasing vacancy concentration, defect agglomeration can form extended line defects such as a row of single vacancies with preferred orientation without significant atomic reconstruction, as we will show below based on DFT calculations. After prolonged exposure to the plasma to further increase the Se vacancy concentration, the defects in the $PdSe_2$ crystals reorganize along some preferred directions and self-assemble into periodic domains, re-establishing the translational symmetry of the crystal, forming a new $Pd_{17}Se_{15}$ phase. This phenomenon has also been found in other 2D materials with high in-plane anisotropy such as SnSe and borophene.[14,40]

To gain more insight into the defect-mediated phase transformation process, density functional theory (DFT) calculations were carried out to understand the structural phase transformation from $PdSe_2$ to $Pd_{17}Se_{15}$. Known phase diagrams[28] indicate the presence of a PdSe phase for intermediate Se content between $PdSe_2$ and $Pd_{17}Se_{15}$. However, the PdSe phase is not observed experimentally by STEM because PdSe and $Pd_{17}Se_{15}$ have quite close stoichiometry and similar structure as well as a relatively small formation enthalpy difference (see Table S2). Therefore, the transformation between PdSe and $Pd_{17}Se_{15}$ is straightforward (Figure S8) and does not affect our calculations of the transformation kinetic pathway from $PdSe_2$ to $Pd_{17}Se_{15}$. Here, we focus on the large leap from $PdSe_2$ to $Pd_{17}Se_{15}$ (or PdSe), in which approximately half of the Se atoms are removed (also verified by NAES above). An attempt to clarify the evolution requires understanding of the role of the impinging high-energy Ar^+ ions in the creation of defects through the loss of Se atoms in TMDs. The energies required for removing Se atoms one by one in $PdSe_2$ in various scenarios were calculated. Our calculations cover all the possible formation pathways of Se vacancies, and eventually we find the most energy-favorable one (see Supporting Information, Tables S3 and S4, and Figures S8–S12 for detailed analysis). In each $PdSe_2$ layer, the Se vacancy (V_{Se}) pairs preferably form along [100] or [010] as shown in Figure 3a and Figure S11. However, across different $PdSe_2$ layers, the V_{Se} pairs alternatively form along the [023] direction (Figure 3b). From here, it is easy to see the emergence of the PdSe phase from the removal of Se atoms in the blue-shaded areas, along the black lines as shown in Figure S8. Increasing the V_{Se} concentration leads to the formation of the $Pd_{17}Se_{15}$ phase, thereby creating a clear and sharp interface at the $PdSe_2/Pd_{17}Se_{15}$ transition region as shown in Figure 3b, which is in excellent agreement with the STEM image (Figure 2e). The formation of the $Pd_{17}Se_{15}$ phase from $PdSe_2$ comes with a concomitant theoretical lattice reduction of ~33% along the direction normal to the surface as shown in Figure S13, which affects the thickness seen in the height profile before and after plasma treatment.

It is interesting to note that the electronic density of states (DOS) and band structures shown in Figure S14 reveal $Pd_{17}Se_{15}$ to be a very good metal with large DOS near the Fermi level. This metallic property coupled with the presence of a sharp atomic interface at the $PdSe_2/Pd_{17}Se_{15}$ boundary region makes $Pd_{17}Se_{15}$ a strong candidate for a contact electrode in $PdSe_2$ devices. Therefore, we converted $PdSe_2$ to the $Pd_{17}Se_{15}$ phase to serve as source and drain electrodes connected to a semiconducting $PdSe_2$ region that was protected from conversion by the plasma treatment (Figure 4a) to investigate the heterophase contact properties in back-gated $Pd_{17}Se_{15}$–$PdSe_2$–$Pd_{17}Se_{15}$ field-effect transistors. Each phase was connected to the two Ti/Au electrodes patterned by e-beam lithography so that local characterization of each phase

DOI: 10.1021/jacs.9b02593
J. Am. Chem. Soc. 2019, 141, 8928–8936

was possible, within and across each phase, using the back-gated device geometry (Figure 4b). Therefore, both kinds of electrical contacts were formed on the same $PdSe_2$ channel for direct device performance comparison.

First, as the output curves show in Figure S15, $Pd_{17}Se_{15}$ is metallic without any gate-bias dependence. The $PdSe_2$ device with $Pd_{17}Se_{15}$ contacts showed linear output curves (nonlinear $I_{ds}-V_{ds}$ curves were produced by the $PdSe_2$ device with Ti/Au contacts). This indicates good Ohmic contact between the two Pd−Se phases. The rectifying behavior of the $I_{ds}-V_{ds}$ curves across the $PdSe_2/Pd_{17}Se_{15}$ heterojunction confirms the presence of a metal−semiconductor interface. In addition, the contact resistances of $PdSe_2$/Ti−Au and $PdSe_2/Pd_{17}Se_{15}$/Ti−Au were measured using the transfer-length method (TLM).[11] As shown in Figure S16, we find a substantial reduction from 2.09 to 0.75 kΩ μm in the contact resistance for phase-transformed-contact devices compared to that for the Ti/Au-contact devices.

We also compared the transfer curves (Figure 4c) and found that the $Pd_{17}Se_{15}$ device showed no gate dependence, further confirming the metallic nature of $Pd_{17}Se_{15}$. The $PdSe_2$ devices with $Pd_{17}Se_{15}$ contacts show preferred n-type semiconducting behavior with significant enhancement of the device performance such as an increased on-state current and transconductance over the one with Ti/Au electrodes. Figure 4d shows the field-effect electron mobility at different temperatures for $PdSe_2$ channels with Ti/Au contacts and $Pd_{17}Se_{15}$ contacts, respectively. The figure clearly shows that the electron mobility is enhanced by a factor of ∼20 in thick flakes compared to that of the device with a conventional metal contact. Note that the on/off ratio of the device is low, which is consistent with our previous observation because the thick $PdSe_2$ flakes have smaller band gaps.[20] We also made similar devices with thin $PdSe_2$ flakes (Figure S17) and found that the mobility is enhanced only by a factor of ∼1.5. The formation of an Ohmic contact at the $PdSe_2/Pd_{17}Se_{15}$ heterojunction is thought to be the origin of the improvement in device performance, by reducing the Schottky barrier. The energy barrier height for $PdSe_2$ devices with and without a $Pd_{17}Se_{15}$ interface were extracted from temperature-dependent electrical measurements (details in the Supporting Information). Figure 4e shows the slope (obtained from the $\log(I_{ds})$ vs $1000/T$ Arrhenius plots shown in Figure S18) at different drain voltages, which confirms the substantial reduction in the energy barrier height for the $PdSe_2$ device with phase-patterned contacts. The Schottky barrier height (SBH) of the Ti/Au-contacted device was measured to be ∼96.2 meV at the flat-band condition. In the same manner, the SBH was extracted to be ∼3.3 meV for devices with $Pd_{17}Se_{15}$ contact, thereby suggesting the formation of desired Ohmic contacts as illustrated in Figure 4f. Table S5 shows the SBHs comparison for several devices with and without $Pd_{17}Se_{15}$ interfacial contact for statistical purposes. The low contact resistance of ∼0.75 kΩ μm and the low SBH of ∼3.3 meV in $PdSe_2$ device with seamless $Pd_{17}Se_{15}$ contacts is comparable or better than those achieved in previously reported 1T phase-contacted TMD devices (see Table S6),[2,12] thus potentially pushing the contact resistance of TMD-based devices closer to the quantum limit.[41]

CONCLUSION

In summary, we have demonstrated the Ar-plasma-induced phase transformation of layered semiconducting $PdSe_2$ to the nonlayered metallic $Pd_{17}Se_{15}$ phase. Cross-sectional STEM images combined with DFT calculations revealed that progressively increasing the concentration of Se vacancies under plasma irradiation triggers the phase transformation. The STEM results also show that planes of the $Pd_{17}Se_{15}$ phase are aligned with the original $PdSe_2$ phase, thereby resulting in atomically sharp interfaces. Unlike the commonly observed layered hexagonal TMDs, Se-vacancy formation in $PdSe_2$ breaks the symmetry of the Se−Se dumbbell, inducing a large structural distortion that gives rise to the formation of the $Pd_{17}Se_{15}$ phase due to the very low interlayer and intralayer defect diffusion barriers in highly anisotropic $PdSe_2$. Through the spatially selective phase conversion of semiconducting $PdSe_2$ to the metallic $Pd_{17}Se_{15}$ phase using an Ar-plasma treatment, atomically sharp junctions were formed and used as seamless contacts for prototype $PdSe_2$ field-effect transistor devices. The contact significantly reduces the SBH (∼3.3 meV) and contact resistance (∼0.75 kΩ μm), resulting in a 20-fold improvement of the carrier mobility and yielding one of the best reported electrical contacts with TMDs. Also, $Pd_{17}Se_{15}$ has other properties (e.g., superconductivity) that could be taken advantage of in making seamless Josephson junctions (superconducting $Pd_{17}Se_{15}$/semiconductor $PdSe_2$) for highly integrable circuit elements in quantum electrodynamics systems.[42] Thus, this scalable, defect-mediated phase-engineering approach provides a pathway for making reliable electrical contacts to enable next-generation electronic devices. In addition, this work demonstrates that defects in highly anisotropic 2D materials can induce new crystalline phases with different stoichiometries to modulate their properties, blurring the traditional distinctions between perfect and defective crystals. Understanding the mechanisms by which multiple nonequilibrium processing methods induce phase transformations between the rich electronic phases (semiconducting, metallic, superconducting, and topological states), diverse polymorphisms (2H, 1T, and pyrite), and various Pd−Se binary phases (e.g., Pd_2Se_3, PdSe, $Pd_{17}Se_{15}$, Pd_7Se_4, and as yet unexplored) related to $PdSe_2$ will enable the exploration of lateral 2D heterostructures for studies of emerging quantum states such as Weyl and Dirac semimetals and topological superconductivity.

EXPERIMENTAL SECTION

$PdSe_2$ Preparation and Plasma Processing. Thin $PdSe_2$ flakes were fabricated by mechanical exfoliation from bulk $PdSe_2$ single crystals and transferred onto a SiO_2 (280 nm)/Si substrate. The exfoliated $PdSe_2$ flakes were characterized by optical microscopy (Nikon LV150), scanning electron microscopy (Zeiss, Merlin, SEM), atomic force microscopy (Bruker, AFM), and Raman spectroscopy (T64000, JY Horiba). Ar-plasma treatment was conducted using a reactive ion etch (RIE) system (Oxford Plasmalab 100), equipped with an inductively coupled plasma (ICP) source with a 13.56 MHz RF generator. The as-prepared sample was placed at the center of a plasma chamber and the pressure in the chamber was maintained at approximately 3 mTorr during sample treatment by flowing argon at 25 standard cubic centimeters per minute (sccm) under pumping. The RF power was controlled from 10 to 50 W depending on the experimental conditions as we discussed in detail (see Supporting Information). The plasma treatment time was varied from 1 to 40 s and was carried out at room temperature. The tunable Ar ion density and energy of the plasma enable a controllable plasma processing of $PdSe_2$ crystals for phase transition studies in this material.

Phase-Patterning Process. To fabricate phase-patterned contact areas, the central regions of pristine samples were protected using poly(methyl methacrylate) (PMMA). The unmasked regions were

DOI: 10.1021/jacs.9b02593
J. Am. Chem. Soc. 2019, 141, 8928−8936

exposed to Ar^+ plasma, which resulted in a structural transformation. After plasma irradiation, the samples were rinsed in acetone and isopropanol to remove the PMMA.

Raman Spectroscopy. Raman measurements were performed using a triple spectrometer (Jobin-Yvon T64000) consisting of a double monochromator coupled to a third monochromator stage with three 1800 grooves/mm gratings equipped with a liquid-nitrogen-cooled CCD detector. All measurements were performed under a microscope in a backscattering configuration. A 532 nm laser (Excelsior, Spectra-Physics) light was focused onto the $PdSe_2$ flakes transferred on the SiO_2/Si wafer with a 100× objective to a spot size of about 1 μm. The excitation laser power on the sample was ~0.5 mW. Averaging between Stokes and anti-Stokes peak positions was used to determine the absolute Raman shifts.

Auger spectra and elemental maps were obtained using a Phi-680 Scanning Auger Nanoprobe. The Nanoprobe uses a field emission (Schottky) electron gun focused to approximately 15 nm in diameter. Auger electrons are energy-analyzed using a double-pass cylindrical mirror analyzer.

STEM Characterization. The thin flakes of $PdSe_2$ obtained by mechanical exfoliation from bulk crystals were released from a SiO_2 substrate by etching with KOH. The released flakes were transferred to TEM grids spin-coated with PMMA. The annular dark-field (ADF) images and annular bright-field (ABF) images were collected using a Nion UltraSTEM200 microscope operated at 200 kV. Additional ADF images were taken using a Nion UltraSTEM100 microscope operated at 60 kV. The as-recorded images were filtered using a Gaussian function (full-width half-maximum = 0.12 nm) to remove high-frequency noise. The convergence half angle of the electron beam was set to 30 mrad and the collection inner half angles of the ADF detector were set to 80 mrad for Nion UltraSTEM200 and 50 mrad for Nion UltraSTEM100. The samples were baked in vacuum at 140 °C overnight before STEM observation. The cross-section sample was prepared using a focused ion beam microscope.

DFT Calculations. Density functional theory calculations were carried out using the Vienna Ab Initio Simulation Package (VASP).[43] The formation enthalpies of all the materials including Pd metal, Se, PdSe, $Pd_{17}Se_{15}$, and $PdSe_2$ with/without vacancies are calculated by using the same pseudopotential and exchange correlation functionals, that is, the projector augmented wave method (PAW)[44] with the generalized gradient approximation of Perdew, Burke, and Ernzerhof (GGA-PBE).[45] The effects of the local-density-approximation (LDA) electronic exchange-correlation functional and the van der Waals functionals optB86b-vdW and optB88-vdW are studied for lattice constants. For all the materials, the atoms are relaxed using a convergence threshold of 1×10^{-7} eV for the total energy and 10^{-5} eV $Å^{-1}$ for the forces on each atom. The plane-wave energy cutoff is 500 eV.

Device Fabrication. The back-gated $PdSe_2$ field-effect transistors were fabricated on a highly doped silicon substrate with 280 nm SiO_2 layer as a dielectric layer using electron beam lithography (FEI DB-FIB with Raith pattern software). As discussed above, the selective areas of individual $PdSe_2$ crystals were treated by Ar plasma before metal deposition. Then the Ti/Au metal contacts (5 nm Ti/30 nm Au) were patterned on the plasma-treated area and untreated $PdSe_2$ surface, respectively. Note that both of the two different types of devices were fabricated on the same $PdSe_2$ flakes for better comparison. The FET device measurements were conducted in a cryogenic probe station using a Keithley 4200 semiconductor analyzer in a two-terminal configuration.

■ ASSOCIATED CONTENT

Supporting Information

The Supporting Information is available free of charge on the ACS Publications website at DOI: 10.1021/jacs.9b02593.

Detailed descriptions of the material processing and characterizations including bulk crystal growth, Ar-plasma treatment, additional AFM, STEM, Raman, FET device performance, and detailed theoretical calculations of the electronic structure, defect, and phase transformation (PDF)

■ AUTHOR INFORMATION

Corresponding Author

*xiaok@ornl.gov (K.X.)

ORCID

Shize Yang: 0000-0002-0421-006X
Tianli Feng: 0000-0002-7284-5657
Raymond R. Unocic: 0000-0002-1777-8228
Kai Xiao: 0000-0002-0402-8276

Author Contributions

#A.D.O., S.Y., and T.F. contributed equally to this work.

Notes

The authors declare no competing financial interest.

■ ACKNOWLEDGMENTS

This work was supported by the U.S. Department of Energy, Office of Science, Basic Energy Sciences, Materials Sciences and Engineering Division. The device fabrication and characterization were conducted at the Center for Nanophase Materials Sciences (CNMS), which is a DOE Office of Science User Facility. A.O. acknowledges fellowship support from the UT/ORNL Bredesen Center for Interdisciplinary Research and Graduate Education. A.H. and D.M. acknowledge support from the Gordon and Betty Moore Foundation's EPiQS Initiative through Grant No. GBMF4416. This research used resources of the National Energy Research Scientific Computing Center (NERSC), a DOE Office of Science User Facility. Theoretical work by T.L.F. and S.T.P. is supported in part by the Department of Energy Grant DE-FG0209ER46554 and by the McMinn Endowment. Computations at Vanderbilt University and ORNL were performed at NERSC funded through Contract No. DE-AC02-05CH11231. Computations also used the Extreme Science and Engineering Discovery Environment (XSEDE) resources. The electron microscopy (S.Z.Y. and M.F.C.) was supported in part by the U.S. Department of Energy, Office of Science, Basic Energy Sciences, Materials Sciences and Engineering Division and through a user proposal supported by ORNL's Center for Nanophase Materials Sciences, which is sponsored by the Scientific User Facilities Division of the U.S. Department of Energy.

■ REFERENCES

(1) Iannaccone, G.; Bonaccorso, F.; Colombo, L.; Fiori, G. Quantum engineering of transistors based on 2D materials heterostructures. *Nat. Nanotechnol.* **2018**, *13* (3), 183−191.

(2) Allain, A.; Kang, J. H.; Banerjee, K.; Kis, A. Electrical contacts to two-dimensional semiconductors. *Nat. Mater.* **2015**, *14* (12), 1195−1205.

(3) Das, S.; Chen, H. Y.; Penumatcha, A. V.; Appenzeller, J. High Performance Multilayer MoS_2 Transistors with Scandium Contacts. *Nano Lett.* **2013**, *13* (1), 100−105.

(4) Popov, I.; Seifert, G.; Tomanek, D. Designing Electrical Contacts to MoS_2 Monolayers: A Computational Study. *Phys. Rev. Lett.* **2012**, *108* (15), 156802.

(5) Kang, J. H.; Liu, W.; Sarkar, D.; Jena, D.; Banerjee, K. Computational Study of Metal Contacts to Monolayer Transition-Metal Dichalcogenide Semiconductors. *Phys. Rev. X* **2014**, *4* (3), 031005.

DOI: 10.1021/jacs.9b02593
J. Am. Chem. Soc. 2019, 141, 8928−8936

(6) Liu, Y. Y.; Stradins, P.; Wei, S. H. Van der Waals metal-semiconductor junction: Weak Fermi level pinning enables effective tuning of Schottky barrier. *Sci. Adv.* **2016**, *2* (4), No. e1600069.
(7) Ghorbani-Asl, M.; Kuc, A.; Miro, P.; Heine, T. A Single-Material Logical Junction Based on 2D Crystal PdS_2. *Adv. Mater.* **2016**, *28* (5), 853−856.
(8) Hu, X. H.; Wang, Y. F.; Shen, X. D.; Krasheninnikov, A. V.; Sun, L. T.; Chen, Z. F. 1T phase as an efficient hole injection layer to TMDs transistors: a universal approach to achieve p-type contacts. *2D Mater.* **2018**, *5* (3), 031012.
(9) Liu, Y.; Wu, H.; Cheng, H. C.; Yang, S.; Zhu, E. B.; He, Q. Y.; Ding, M. N.; Li, D. H.; Guo, J.; Weiss, N. O.; Huang, Y.; Duan, X. F. Toward Barrier Free Contact to Molybdenum Disulfide Using Graphene Electrodes. *Nano Lett.* **2015**, *15* (5), 3030−3034.
(10) Leong, W. S.; Luo, X.; Li, Y. D.; Khoo, K. H.; Quek, S. Y.; Thong, J. T. L. Low Resistance Metal Contacts to MoS_2 Devices with Nickel-Etched-Graphene Electrodes. *ACS Nano* **2015**, *9* (1), 869−877.
(11) Kappera, R.; Voiry, D.; Yalcin, S. E.; Branch, B.; Gupta, G.; Mohite, A. D.; Chhowalla, M. Phase-engineered low-resistance contacts for ultrathin MoS_2 transistors. *Nat. Mater.* **2014**, *13* (12), 1128−1134.
(12) Cho, S.; Kim, S.; Kim, J. H.; Zhao, J.; Seok, J.; Keum, D. H.; Baik, J.; Choe, D. H.; Chang, K. J.; Suenaga, K.; Kim, S. W.; Lee, Y. H.; Yang, H. Phase patterning for Ohmic homojunction contact in $MoTe_2$. *Science* **2015**, *349* (6248), 625−628.
(13) Zhu, J. Q.; Wang, Z. C.; Yu, H.; Li, N.; Zhang, J.; Meng, J. L.; Liao, M. Z.; Zhao, J.; Lu, X. B.; Du, L. J.; Yang, R.; Shi, D.; Jiang, Y.; Zhang, G. Y. Argon Plasma Induced Phase Transition in Monolayer MoS_2. *J. Am. Chem. Soc.* **2017**, *139* (30), 10216−10219.
(14) Sutter, E.; Huang, Y.; Komsa, H. P.; Ghorbani-Asl, M.; Krasheninnikov, A. V.; Sutter, P. Electron-Beam Induced Transformations of Layered Tin Dichalcogenides. *Nano Lett.* **2016**, *16* (7), 4410−4416.
(15) Lin, J. H.; Zuluaga, S.; Yu, P.; Liu, Z.; Pantelides, T.; Suenaga, K. Novel Pd_2Se_3 Two-Dimensional Phase Driven by Interlayer Fusion in Layered $PdSe_2$. *Phys. Rev. Lett.* **2017**, *119* (1), 016101.
(16) Stanford, M. G.; Pudasaini, P. R.; Gallmeier, E. T.; Cross, N.; Liang, L.; Oyedele, A.; Duscher, G.; Mahjouri-Samani, M.; Wang, K.; Xiao, K.; Geohegan, D. B.; Belianinov, A.; Sumpter, B. G.; Rack, P. D. High Conduction Hopping Behavior Induced in Transition Metal Dichalcogenides by Percolating Defect Networks: Toward Atomically Thin Circuits. *Adv. Funct. Mater.* **2017**, *27* (36), 1702829.
(17) Wang, Y.; Xiao, J.; Zhu, H. Y.; Li, Y.; Alsaid, Y.; Fong, K. Y.; Zhou, Y.; Wang, S. Q.; Shi, W.; Wang, Y.; Zettl, A.; Reed, E. J.; Zhang, X. Structural phase transition in monolayer $MoTe_2$ driven by electrostatic doping. *Nature* **2017**, *550* (7677), 487.
(18) Gong, Y. J.; Yuan, H. T.; Wu, C. L.; Tang, P. Z.; Yang, S. Z.; Yang, A. K.; Li, G. D.; Liu, B. F.; van de Groep, J.; Brongersma, M. L.; Chisholm, M. F.; Zhang, S. C.; Zhou, W.; Cui, Y. Spatially controlled doping of two-dimensional SnS_2 through intercalation for electronics. *Nat. Nanotechnol.* **2018**, *13* (4), 294.
(19) Sung, J. H.; Heo, H.; Si, S.; Kim, Y. H.; Noh, H. R.; Song, K.; Kim, J.; Lee, C. S.; Seo, S. Y.; Kim, D. H.; Kim, H. K.; Yeom, H. W.; Kim, T. H.; Choi, S. Y.; Kim, J. S.; Jo, M. H. Coplanar semiconductor-metal circuitry defined on few-layer $MoTe_2$ via polymorphic heteroepitaxy. *Nat. Nanotechnol.* **2017**, *12* (11), 1064.
(20) Oyedele, A. D.; Yang, S. Z.; Liang, L. B.; Puretzky, A. A.; Wang, K.; Zhang, J. J.; Yu, P.; Pudasaini, P. R.; Ghosh, A. W.; Liu, Z.; Rouleau, C. M.; Sumpter, B. G.; Chisholm, M. F.; Zhou, W.; Rack, P. D.; Geohegan, D. B.; Xiao, K. $PdSe_2$: Pentagonal Two-Dimensional Layers with High Air Stability for Electronics. *J. Am. Chem. Soc.* **2017**, *139* (40), 14090−14097.
(21) Chow, W. L.; Yu, P.; Liu, F. C.; Hong, J. H.; Wang, X. L.; Zeng, Q. S.; Hsu, C. H.; Zhu, C.; Zhou, J. D.; Wang, X. W.; Xia, J.; Yan, J. X.; Chen, Y.; Wu, D.; Yu, T.; Shen, Z. X.; Lin, H.; Jin, C. H.; Tay, B. K.; Liu, Z. High Mobility 2D Palladium Diselenide Field-Effect Transistors with Tunable Ambipolar Characteristics. *Adv. Mater.* **2017**, *29* (21), 1602969.
(22) Selb, E.; Tribus, M.; Heymann, G. Verbeekite, the Long-Unknown Crystal Structure of Monoclinic $PdSe_2$. *Inorg. Chem.* **2017**, *56* (10), 5885−5891.
(23) Lei, W.; Zhang, S.; Heymann, G.; Tang, X.; Wen, J.; Zheng, X.; Hu, G.; Ming, X. A New 2D High-Pressure Phase of $PdSe_2$ with High-Mobility Transport Anisotropy for Photovoltaic Applications. *J. Mater. Chem. C* **2019**, *7* (7), 2096−2105.
(24) Miro, P.; Ghorbani-Asl, M.; Heine, T. Two Dimensional Materials Beyond MoS_2: Noble-Transition-Metal Dichalcogenides. *Angew. Chem., Int. Ed.* **2014**, *53* (11), 3015−3018.
(25) Noh, H. J.; Jeong, J.; Cho, E. J.; Kim, K.; Min, B. I.; Park, B. G. Experimental Realization of Type-II Dirac Fermions in a $PdTe_2$ Superconductor. *Phys. Rev. Lett.* **2017**, *119* (1), 016401.
(26) Bahramy, M. S.; Clark, O. J.; Yang, B. J.; Feng, J.; Bawden, L.; Riley, J. M.; Markovic, I.; Mazzola, F.; Sunko, V.; Biswas, D.; Cooil, S. P.; Jorge, M.; Wells, J. W.; Leandersson, M.; Balasubramanian, T.; Fujii, J.; Vobornik, I.; Rault, J. E.; Kim, T. K.; Hoesch, M.; Okawa, K.; Asakawa, M.; Sasagawa, T.; Eknapakul, T.; Meevasana, W.; King, P. D. C. Ubiquitous formation of bulk Dirac cones and topological surface states from a single orbital manifold in transition-metal dichalcogenides. *Nat. Mater.* **2018**, *17* (1), 21.
(27) ElGhazali, M. A.; Naumov, P. G.; Mirhosseini, H.; Suss, V.; Muchler, L.; Schnelle, W.; Felser, C.; Medvedev, S. A. Pressure-induced superconductivity up to 13.1 K in the pyrite phase of palladium diselenide $PdSe_2$. *Phys. Rev. B: Condens. Matter Mater. Phys.* **2017**, *96* (6), 060509.
(28) Takabatake, T.; Ishikawa, M.; Jorda, J. L. Superconductivity and Phase-Relations in the Pd-Se System. *J. Less-Common Met.* **1987**, *134* (1), 79−89.
(29) Hulliger, F. Electrical Properties of Some Nickel-Group Chalcogenides. *J. Phys. Chem. Solids* **1965**, *26* (3), 639.
(30) Naren, H. R.; Thamizhavel, A.; Auluck, S.; Prasad, R.; Ramakrishnan, S. Normal state and superconducting properties of $Rh_{17}S_{15}$ and $Pd_{17}Se_{15}$. *Supercond. Sci. Technol.* **2011**, *24* (10), 105015.
(31) Chang, G. Q.; Wieder, B. J.; Schindler, F.; Sanchez, D. S.; Belopolski, I.; Huang, S. M.; Singh, B.; Wu, D.; Chang, T. R.; Neupert, T.; Xu, S. Y.; Lin, H.; Hasan, M. Z. Topological quantum properties of chiral crystals. *Nat. Mater.* **2018**, *17* (11), 978.
(32) Nguyen, G. D.; Liang, L. B.; Zou, Q.; Fu, M. M.; Oyedele, A. D.; Sumpter, B. G.; Liu, Z.; Gai, Z.; Xiao, K.; Li, A. P. 3D Imaging and Manipulation of Subsurface Selenium Vacancies in $PdSe_2$. *Phys. Rev. Lett.* **2018**, *121* (8), 086101.
(33) Zuluaga, S.; Lin, J. H.; Suenaga, K.; Pantelides, S. T. Two-dimensional $PdSe_2$-Pd_2Se_3 junctions can serve as nanowires. *2D Mater.* **2018**, *5* (3), 035025.
(34) Zhang, S. H.; Liu, B. G. Hole-doping-induced half-metallic ferromagnetism in a highly-air-stable $PdSe_2$ monolayer under uniaxial stress. *J. Mater. Chem. C* **2018**, *6* (25), 6792−6798.
(35) Kim, J. H.; Yun, S. J.; Lee, H. S.; Zhao, J.; Bouzid, H.; Lee, Y. H. Plasma-Induced Phase Transformation of SnS_2 to SnS. *Sci. Rep.* **2018**, *8*, 10284.
(36) Pudasaini, P. R.; Oyedele, A.; Zhang, C.; Stanford, M. G.; Cross, N.; Wong, A. T.; Hoffman, A. N.; Xiao, K.; Duscher, G.; Mandrus, D. G.; Ward, T. Z.; Rack, P. D. High-performance multilayer WSe_2 field-effect transistors with carrier type control. *Nano Res.* **2018**, *11* (2), 722−730.
(37) Liu, Y. L.; Nan, H. Y.; Wu, X.; Pan, W.; Wang, W. H.; Bai, J.; Zhao, W. W.; Sun, L. T.; Wang, X. R.; Ni, Z. H. Layer-by-Layer Thinning of MoS_2 by Plasma. *ACS Nano* **2013**, *7* (5), 4202−4209.
(38) Puretzky, A. A.; Oyedele, A. D.; Xiao, K.; Haglund, A. V.; Sumpter, B. G.; Mandrus, D.; Geohegan, D. B.; Liang, L. B. Anomalous interlayer vibrations in strongly coupled layered $PdSe_2$. *2D Mater.* **2018**, *5* (3), 035016.
(39) Mahjouri-Samani, M.; Liang, L. B.; Oyedele, A.; Kim, Y. S.; Tian, M. K.; Cross, N.; Wang, K.; Lin, M. W.; Boulesbaa, A.; Rouleau, C. M.; Puretzky, A. A.; Xiao, K.; Yoon, M.; Eres, G.; Duscher, G.; Sumpter, B. G.; Geohegan, D. B. Tailoring Vacancies Far Beyond Intrinsic Levels Changes the Carrier Type and Optical Response in Monolayer $MoSe_{2-x}$ Crystals. *Nano Lett.* **2016**, *16* (8), 5213−5220.

DOI: 10.1021/jacs.9b02593
J. Am. Chem. Soc. 2019, 141, 8928−8936

(40) Liu, X. L.; Zhang, Z. H.; Wang, L. Q.; Yakobson, B. I.; Hersam, M. C. Intermixing and periodic self-assembly of borophene line defects. *Nat. Mater.* **2018**, *17* (9), 783.
(41) Jena, D.; Banerjee, K.; Xing, G. H. 2D CRYSTAL SEMICONDUCTORS Intimate contacts. *Nat. Mater.* **2014**, *13* (12), 1076−1078.
(42) Wang, J. I.-J.; Rodan-Legrain, D.; Bretheau, L.; Campbell, D. L.; Kannan, B.; Kim, D.; Kjaergaard, M.; Krantz, P.; Samach, G. O.; Yan, F. Coherent control of a hybrid superconducting circuit made with graphene-based van der Waals heterostructures. *Nat. Nanotechnol.* **2019**, *14*, 120−125.
(43) Kresse, G.; Hafner, J. Abinitio Molecular-Dynamics for Liquid-Metals. *Phys. Rev. B: Condens. Matter Mater. Phys.* **1993**, *47* (1), 558−561.
(44) Kresse, G.; Furthmuller, J. Efficient iterative schemes for ab initio total-energy calculations using a plane-wave basis set. *Phys. Rev. B: Condens. Matter Mater. Phys.* **1996**, *54* (16), 11169−11186.
(45) Perdew, J. P.; Burke, K.; Ernzerhof, M. Generalized gradient approximation made simple. *Phys. Rev. Lett.* **1996**, *77* (18), 3865−3868.

DOI: 10.1021/jacs.9b02593
J. Am. Chem. Soc. 2019, 141, 8928−8936

Supporting Information

Defect-mediated phase transformation in anisotropic 2D $PdSe_2$ crystals for seamless electrical contacts

Akinola D. Oyedele[1,2,†], Shize Yang[3,†], Tianli Feng[3,4,†], Amanda V. Haglund[2,5], Yiyi Gu[1,6], Alexander A. Puretzky[1], Dayrl Briggs[1], Christopher M. Rouleau[1], Matthew F. Chisholm[3], Raymond R. Unocic[1], David Mandrus[3,5], Harry M. Meyer III[1], Sokrates T. Pantelides[3,4], David B. Geohegan[1], Kai Xiao[1,2]*

[1]Center for Nanophase Materials Sciences, Oak Ridge National Laboratory, Oak Ridge, TN, USA. [2]Bredesen Center for Interdisciplinary and Graduate Education, University of Tennessee, Knoxville, TN, USA. [3]Materials Science and Technology Division, Oak Ridge National Laboratory, Oak Ridge, TN, USA. [4]Department of Physics and Astronomy and Department of Electrical Engineering and Computer Science, Vanderbilt University, Nashville, TN, USA. [5]Department of Materials Science and Engineering, University of Tennessee, Knoxville, TN, USA. [6]Key Laboratory of Photochemical Conversion and Optoelectronic Materials, Technical Institute of Physics and Chemistry, Chinese Academy of Sciences, Beijing, P. R. China.

Table of contents

1. Materials Processing and Characterization
    A. $PdSe_2$ bulk crystal growth
    B. Structural transformation via Ar^+ plasma treatment
    C. Atomic force microscopy (AFM) and Raman spectroscopy
    D. Nano-Auger electron spectroscopy (NAES)
2. Scanning transmission electron microscopy (STEM)
3. Density Functional Theory (DFT) Calculations
4. Field-Effect Transistor (FET) Device
    A. Device fabrication, patterning, and measurement
    B. Schottky-barrier height calculation

1. Materials Processing & Characterizations

A. $PdSe_2$ bulk crystal growth & exfoliation

Bulk $PdSe_2$ crystals were synthesized through the self-flux growth method. Palladium powder (99.995%, Alfa Aesar) and selenium shot (99.999%, Alfa Aesar) were loaded into a crucible in a 1:6 molar ratio, Pd:Se, and then sealed in a fused-quartz tube under vacuum. The tube was placed upright in a muffle furnace, slowly heated to 850 °C over 24 hrs, then held at 850 °C for 50 hrs. The furnace cooling rate was controlled at 3 °C/hr from 850 °C down to 450 °C, then the furnace was allowed to cool to room temperature naturally. Crystals were manually removed by breaking the flux chunk and separating the crystals from the flux.

B. Structural transformation via Ar^+ plasma treatment

An argon plasma from Oxford's inductively coupled plasma (ICP) source was used to treat exfoliated $PdSe_2$ flakes at 20 °C. The source has separate RF and ICP generators which determine both ion density and energy, enabling high process flexibility (see a schematic in Figure S1(a)). To determine the treatment rate, which is related to both thickness reduction and the depth of the new phase, over 20 samples were prepared with varying thicknesses and subjected to the Ar^+ plasma at 50 W RF power for 10 s and 20 s. Figure S1 (b) shows a histogram plotting the frequency of samples with different thickness reduction, which shows an average thinning rate of ~1 nm/s and ~2 nm/s for treatment times of 10 s and 20 s, respectively. From the histograms (a-b) and the corresponding scatter plots (c-d), it is obvious that the treatment rate across the sample is anisotropic, typical of plasma systems. However, we selected 10 s to be reasonably a good treatment time for thicker samples (~25-40 nm), while for thinner samples (10 nm $\leq$ t $\leq$ 25 nm), the plasma treatment time was reduced to 5 s. For sample thicknesses < 10 nm, both the plasma treatment time and power were reduced to an RF power of 25 W and a treatment time of ~ 1-3 s.

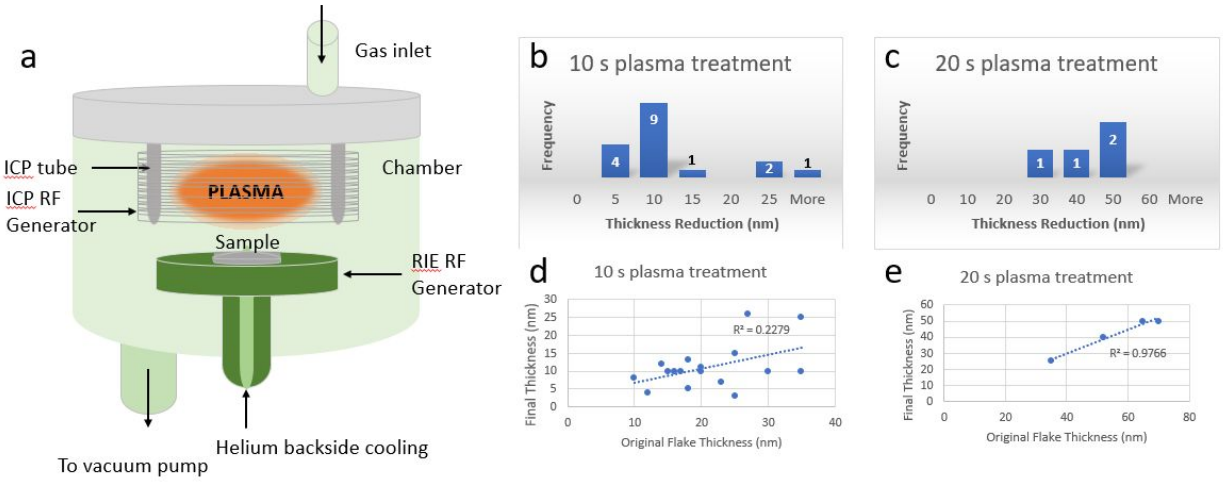

Figure S1. (a) Schematic of the inductively coupled plasma (ICP) system (Oxford Instruments PlasmaLab System100) used for the Ar^+ treatment of $PdSe_2$. (b-e) Statistics show the influence of Ar plasma treatment duration on flake thickness reduction using 50 W RF ICP power. (b-c) Histogram of the number of samples with different thickness reduction for 10 s and 20 s plasma treatment, respectively. Corresponding scatter plots are shown in (d-e), which characterizes the anisotropy of the plasma treatment on samples with different flake locations at shorter durations.

C. Atomic force microscopy (AFM) and Raman Spectroscopy

Using Scotch tape, thin $PdSe_2$ flakes were exfoliated onto a SiO_2 (280 nm-thick)/silicon substrate from the bulk crystal. The locations of suitable flakes were identified using a Nikon LV150 optical microscope. The thickness of the flakes was measured in air by AFM (Bruker® Dimension Icon). The height profile after plasma treatment shows a thickness reduction associated with the structural transformation, which could be as a result of both lattice parameter changes and etching. (Figure S2 (a-b)). Figure S2 (c-d) shows the obtained Raman spectra for the anti-Stokes and Stokes modes for a ~10 nm sample. The red and black curves represent the spectra for the pristine and irradiated samples, respectively. The three main peaks observed correspond to the A_g^1-B_{1g}^1, A_g^2, and A_g^3

modes as defined for $PdSe_2$ in our previous work[1]. The B_{1g}^2 peak is visible in the spectra, although with a lower intensity due to the orientation of the crystal and its anisotropic nature. The B_{1g}^3 peak is on the shoulder of the A_g^3, also with typically lower relative intensity. There is no significant difference between the Raman spectra of $PdSe_2$ before and after irradiation when measured in the high-frequency region (HF, ~ 100 cm^{-1} – 300 cm^{-1}) as shown in Figure S2c. For thinner samples, the HF Raman peak positions remain unaffected, but the intensity is slightly impacted (as shown in Fig. 1e in the main text). Different from the observations in the HF region, in the low-frequency (LF) Raman region (< 60 cm^{-1}), there are significant differences (Figure S2d) including the disappearance of some peaks, and new peaks appearing at a reduced intensity. The strong LF Raman peaks in $PdSe_2$ crystals have been used to characterize interlayer atomic vibrations in the breathing mode, and a model was developed to accurately depict the number of $PdSe_2$ layers and their associated Raman modes.[2] We compared the LF Raman peaks of the flakes shown in Figure S2 before and after plasma treatment in Table S1. The observed LF Raman peaks before plasma treatment corresponds to ~21 L $PdSe_2$. However, after plasma irradiation, the peaks deviate from the established model for $PdSe_2$, thereby suggesting the formation of a new material. It is interesting to note that the emergence of the new phase cannot be predicted with HF Raman spectroscopy, because of the similarity in HF Raman peaks of $PdSe_2$ and $Pd_{17}Se_{15}$ as reported by Kukunuri et. al.[3] Therefore, understanding phase transformation of $PdSe_2$ using Raman spectroscopy will require attention to the LF region.

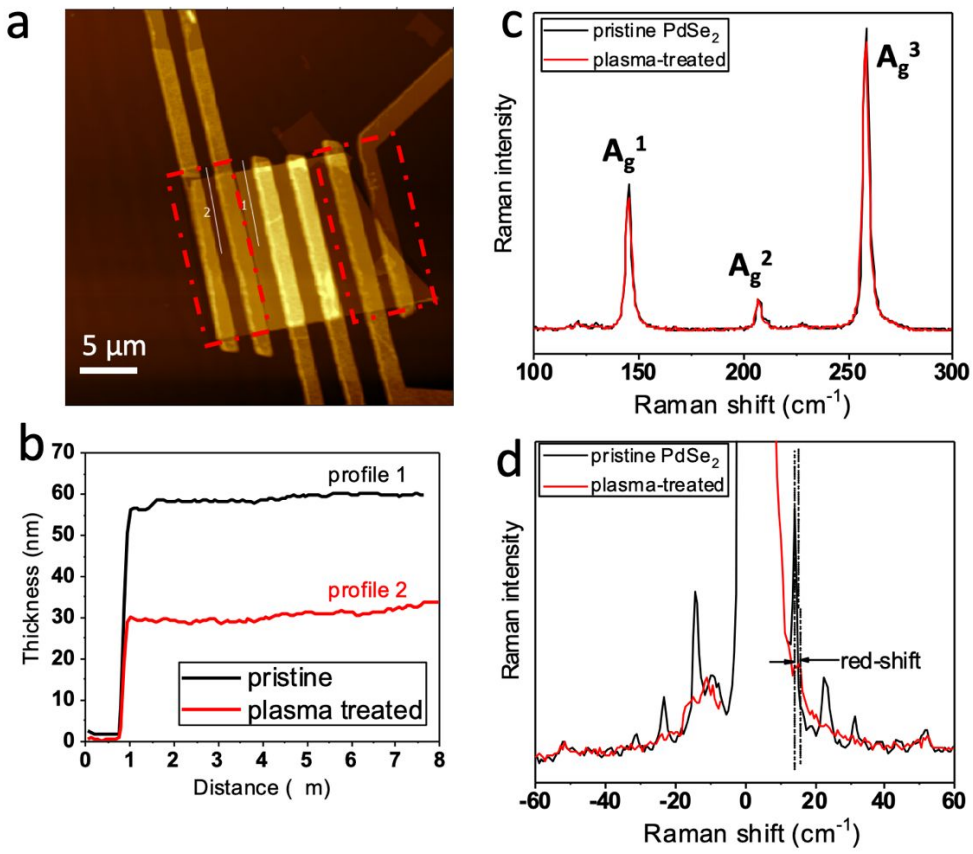

Figure S2. (a) An AFM image of a $PdSe_2$ flake after 10 s Ar plasma treatment. The areas outline in red dashes show the treated regions. (b) Line profiles from lines in Fig (a) show the thickness reduction from ~55 nm to 30 nm after plasma treatment. (c) Stokes and anti-Stokes Raman spectra of pristine and irradiated $PdSe_2$ crystals (10 nm-thick) in the high-frequency (HF) region (d), and low-frequency (LF) region.

Table S1. Comparison of LF-Raman peak positions for pristine and plasma-irradiated $PdSe_2$ crystals.

LF-Raman peaks	B1	B3	B5	B7
Pristine	-	14.3	23.0	31.4
Plasma treated	-	15.4	-	-

D. **Nano-Auger Electron Spectroscopy (NAES)**

Auger spectra and elemental maps were obtained using a Phi-680 scanning Auger nanoprobe. The Nanoprobe uses a field emission (Schottky) electron gun focused to approximately 15 nm in diameter. Auger electrons are energy analyzed using a double pass cylindrical mirror analyzer (CMA). Figure S3 shows Nano-Auger measurement of the chemical composition of the selective patterned heterophase of $PdSe_2$ and $Pd_{17}Se_{15}$ on one flake. As shown in Figure S3 (a) and (b), the heterophase arrays are formed within few-layer crystals by patterning and selective conversion processes. The scanning electron microscopy (SEM) image (Figure S3 (b)) of a sample in which the left side has been exposed to Ar^+ plasma, while the right part has been protected by PMMA through an electron-beam patterning fabrication process. The two red circles are where point-data from the nano-Auger was accumulated using a Survey Scan. Figure S3(e) and (f) show the survey spectra in both direct mode and derivative mode which indicates the presence of Pd, Se, C, Si, and O atoms. The Si atoms originate from the Si/SiO_2 substrate used, while C atoms indicate the presence of carbon residues from the photolithography process. Color maps and color-combined maps for Se + Pd were created from the individual maps. Figure S3 (c) and (d) show the color-combined maps made from the gray-scale images, with a more blueish composition in the irradiated area due to the relative presence of more Pd atoms. The raw map data was processed this way: a smooth function was initially used on each map and then the contrast min/max were stretched to get a visually appealing image, and finally, the brightness was adjusted to minimize the noise level. To analyze the composition of the atoms in each material with improved accuracy, a 2 μm x 1 μm area was chosen around where the point data were taken. This is slightly different from point-data in that the resulting composition is an average of the area contained within the

defined area. Shown in the line profile across the heterophase junction in Figure S3 (d) is the average composition from the two areas, where the Se/Pd ratio of the irradiated area is close to 0.9 which is lower than that of the pristine area (Se/Pd, ~2.0). This shows that the irradiated area has experienced the removal of over half the selenium atoms, which drives the structural transformation similar to those observed in $SnSe_2$. [4]

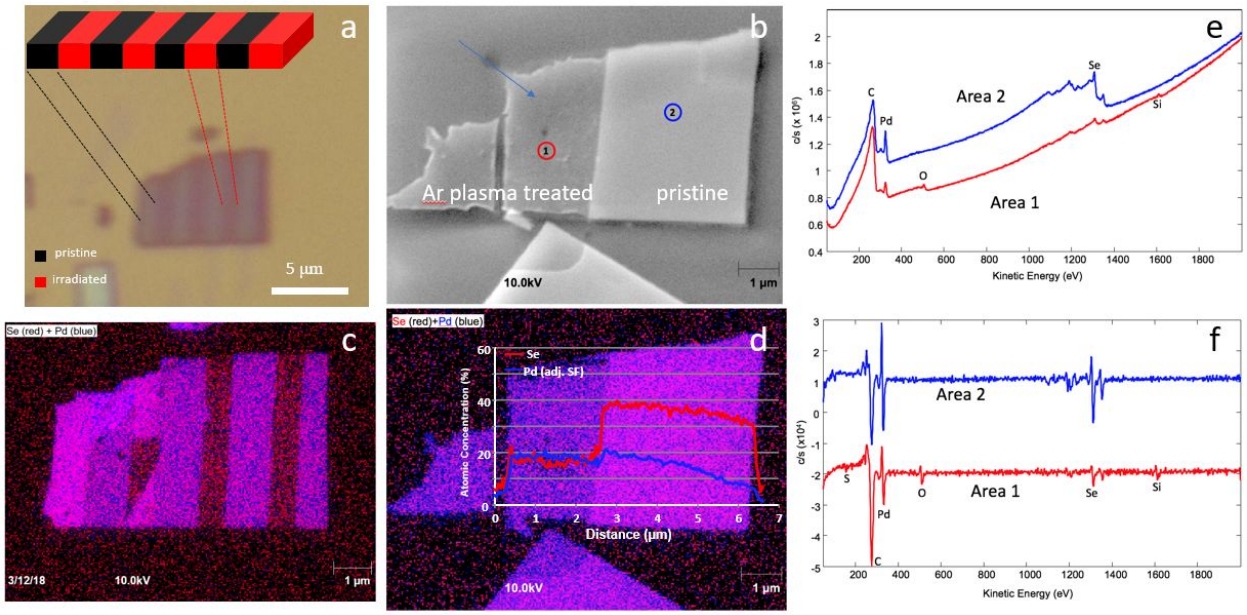

Figure S3. Nano-Auger electron spectroscopy of a $PdSe_2/Pd_{17}Se_{15}$ heterostructure formed within few-layer $PdSe_2$ crystals by selective patterning and Ar-plasma conversion. The black and red areas in (a) represent $PdSe_2$ and $Pd_{17}Se_{15}$, respectively, and (c) shows the nano-Auger electron spectroscopy (NAES) map overlaid with the relative atomic compositions of Se and Pd. The dark regions have relatively higher Pd composition. (b) an SEM image of Ar plasma-treated and pristine regions of $PdSe_2$ crystal. (d) Color maps show an increase in relative Pd composition for the Ar plasma treated areas. Inset shows the relative atomic composition of Se and Pd through a line scan which conforms the loss of Se in the plasma treated region. (e) Survey spectra in both direct mode and (f) derivative mode which indicates the presence of Pd, Se, C, Si, and O atoms.

2. Atomic structure of $Pd_{17}Se_{15}$ and heterophase junction characterization by scanning transmission electron microscopy (STEM)

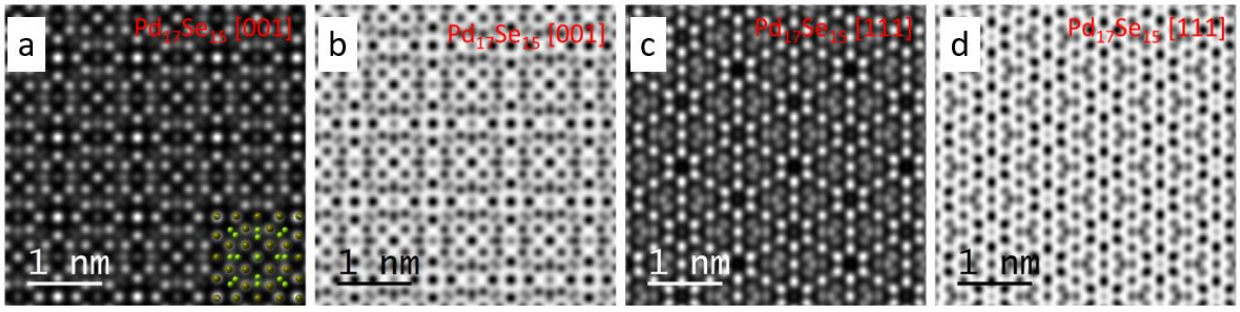

Figure S4. Simulated images with the confirmed structural model. Simulated $Pd_{17}Se_{15}$ phase along [001] zone axis with ADF (a) and ABF (b) mode were shown. Simulated $Pd_{17}Se_{15}$ phase along [111] zone axis with ADF (c) and ABF (d) mode were shown.

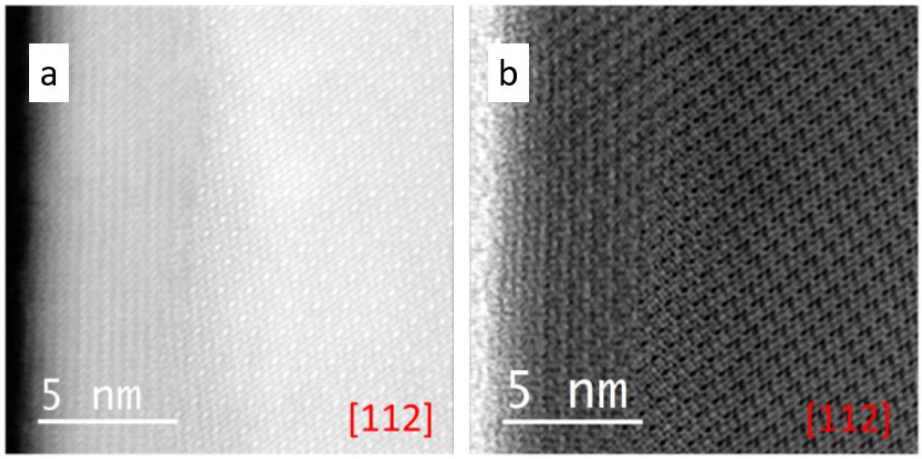

Figure S5. STEM ADF (a) and ABF (b) shows the $Pd_{17}Se_{15}$ structure near the interface along the [112] zone axis.

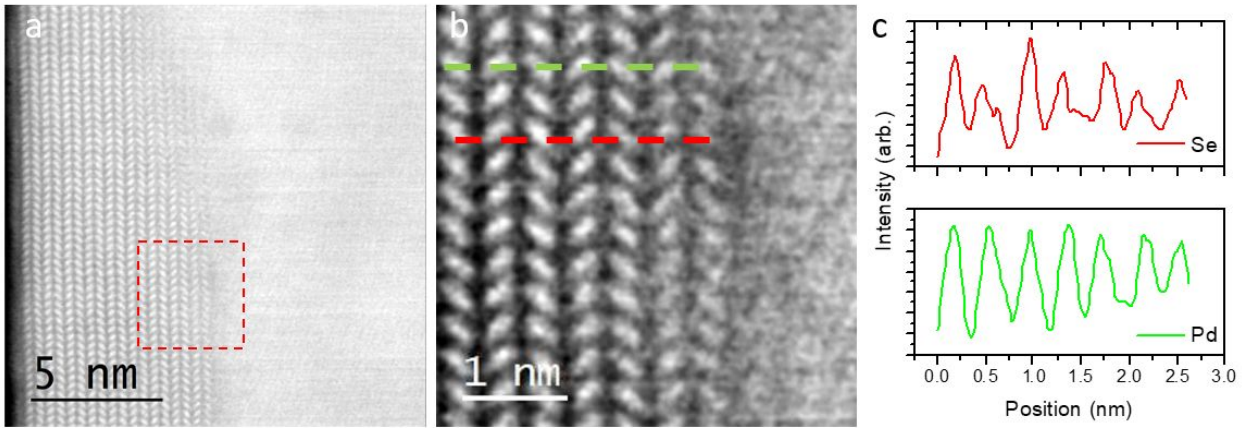

Figure S6. (a) High angle annular dark field image of the $PdSe_2/Pd_{17}Se_{15}$ interface. (b) Enlarged view of the interface region. (c) Line profile of dash line Pd and Se positions in (b).

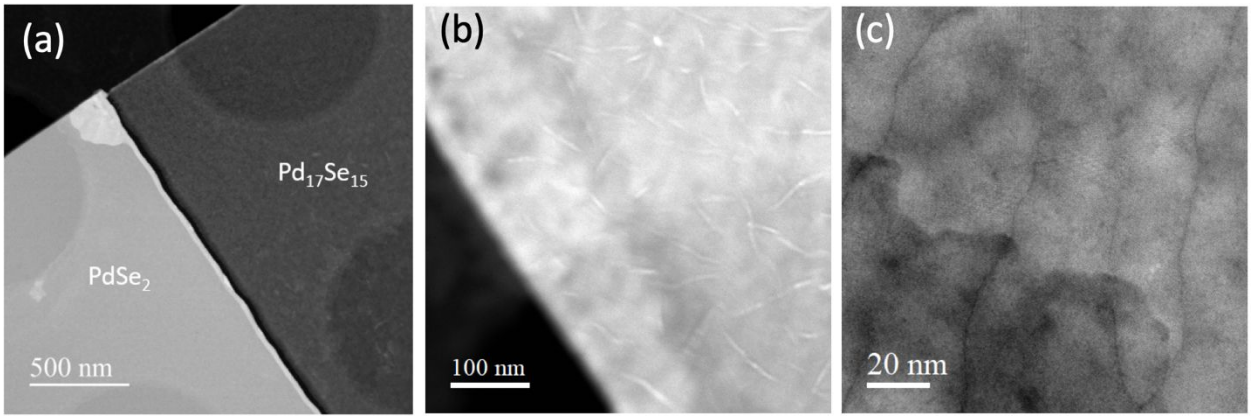

Figure S7. (a) Transmission electron microscopy (TEM) image of the seamless contact region in selectively Ar plasma-treated $PdSe_2$, which shows that the new phase, $Pd_{17}Se_{15}$ is polycrystalline but still retains good crystallinity.

3. Density Functional Theory (DFT) Calculations

The formation enthalpies of $PdSe_2$ and $Pd_{17}Se_{15}$ are calculated via the similar method as Ref 4. Since these compounds as well as Pd and Se metals are all solids, the formation enthalpies are the same as formation energy, which is $xE_{Pd} + yE_{Se} - E_{PdxSey}$ for Pd_xSe_y.

To determine the most likely kinetic pathway of the transformation from $PdSe_2$ to $Pd_{17}Se_{15}$, as shown in **Figure S8**, we calculated the energies that are required for Ar^+ ion to remove Se atoms. To remove one Se atom in $PdSe_2$ layer, it takes 2.37 eV as shown in **Fig. S9a**. The removal of the second Se atom may take the same or less energy depending on the distance of it from the first one. If they are so far away that their removals are independent, it takes the same energy of 2.37 eV/atom as shown in **Fig. S9b**. If the second Se atom is closer, the potential energy between the two Se atoms can compensate partial of the energy that is required to removing two independent Se atoms. As shown in **Figs. S9 (c)** and **(d)**, the energy for removing two Se atoms is reduced from 2.37 eV/atom to 2.35 eV/atom when the two Se are closer, and further to 2.09 eV/atom when they are the nearest neighbors. After figuring out that the removal of nearest neighbors is the most favorable, we calculated the energy required for removing more Se atoms inside each $PdSe_2$ layer. Since we have found that the closer the Se atoms are, the less the energy is needed for the removal, it is naturally considered that the removal of the gathered nearest Se pairs (Fig. S10a) should take the lowest energy. However, we find that the energy can be as high as 2.14 eV/atom. The reason is that the removal of these gathered Se atoms will leave behind isolated Pd atoms, which have much larger energy than bonded atoms. To make sure no Pd atom is left isolated, a possible way is to remove the nearest Se pairs randomly as shown in Fig. S10b, and this is found to take approximately 2 eV/atom, which is only slightly lower than the energy (2.09 eV/atom) for removing one nearest Se pair because these Se pairs are far away, and nearly independent, from

each other. Therefore, to remove the nearest Se pairs that are close enough (but not so close that leave Pd isolated atoms), the most plausible way is to remove nearest Se pairs one by one along the [110] direction as shown in Fig. S10c. We find that the required energy is still as high as 1.98 eV/atom. This high energy is because the removal of Se atoms will leave a gap in which two Pd arrays exposed to each other are subjected to repulsive forces. By this, there is only one plausible configuration left, as shown in Fig. S10d, for which we find that the required energy of Se removal is reduced dramatically to 1.83 eV/atom. The reason is that this configuration satisfies all the three conditions:

1. The nearest Se pairs are not so close that the removal leaves isolated Pd atoms,
2. The nearest Se pairs are not too far way to be dependent,
3. The removal does not leave a gap.

Based on the analysis above, it is natural to figure out a way of removing half the Se atoms in each $PdSe_2$ layer. As shown in Fig. S11, we have listed the four removal configurations that are plausible. It is found that configuration (a) requires the lowest energy, i.e., 1.71 eV/atom, which is much lower than the others which either leave either isolated Pd atoms, gaps, or Se pairs far away from each other.

In the steps above, we have determined the configuration and minimum energy pathway for Se removal inside each $PdSe_2$ layer. Now we investigate the likely mechanisms for Se removal perpendicular to the layer direction, since the Ar^+ beams bombard along the [001] direction layer by layer. Given the Se removal in the first layer, the removal of the second layer could be either staggered or aligned to the first one as shown in Figs. S12 (a) and (b), respectively. We find that the former takes lower energy. By putting the results of intra- and inter-layer Se removal together, the Se transition pathway shown in Fig. S8 is realized. The orientation of $Pd_{17}Se_{15}$ and the interface

between $PdSe_2$ and $Pd_{17}Se_{15}$ show excellent agreement with experimental TEM observations. The intermediate PdSe state could be either included or excluded since its structure and chemical formula are very similar to those of the final state $Pd_{17}Se_{15}$, and the transition between PdSe and $Pd_{17}Se_{15}$ is straightforward.

The choice of pseudopotentials can affect the band gap of $PdSe_2$, which was extensively studied elsewhere. [1,5] Here we have also examined several pseudopotentials and find that irregardless of the exact value of the band gap, the electronic DOS near the Fermi level is significantly smaller than that of $Pd_{17}Se_{15}$.

Table S2. The energy/enthalpy changes of the transformations among $PdSe_2$, PdSe and $Pd_{17}Se_{15}$.

	$PdSe_2$	PdSe	$Pd_{17}Se_{15}$	$PdSe - \frac{1}{19}(2\ PdSe_2 + Pd_{17}Se_{15})$
Formation enthalpy	-0.840 eV	-0.652 eV	-0.601 eV	-0.025 eV

$PdSe_2 + 0.19eV \rightarrow PdSe + Se$

$PdSe + 0.05eV \rightarrow \frac{1}{17} Pd_{17}Se_{15} + \frac{2}{17} Se$

$PdSe_2 + 0.24eV \rightarrow \frac{1}{17} Pd_{17}Se_{15} + \frac{19}{17} Se$

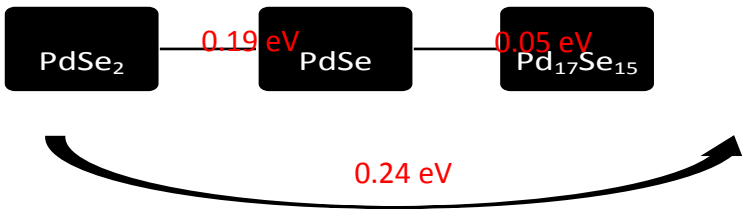

Table S3. The comparison between the lattice constants of $PdSe_2$ from experiment and DFT calculations using several pseudopotentials and van der Waals functionals.

Bulk lattice (Å)	Experiment	DFT				
	Ref [6]	PAW: GGA-PBE	PAW: LDA	+ opt-vdW Ref [1]	GGA + optB86b-vdW	GGA + optB88-vdW
a	5.7457	5.7821	6.1095	5.85	6.0667	5.8403
b	5.8679	5.9340	6.1091	5.99	6.0963	5.9643
c	7.6946	8.5183	6.1107	7.95	6.5704	7.7212

Table S4. The comparison between the lattice constants of $Pd_{17}Se_{15}$ from experiment and DFT using different pseudopotentials.

Bulk lattice (Å)	Experiment Ref 6 [6]	DFT PAW: GGA-PBE	DFT PAW: LDA
a	10.604	10.768	10.541

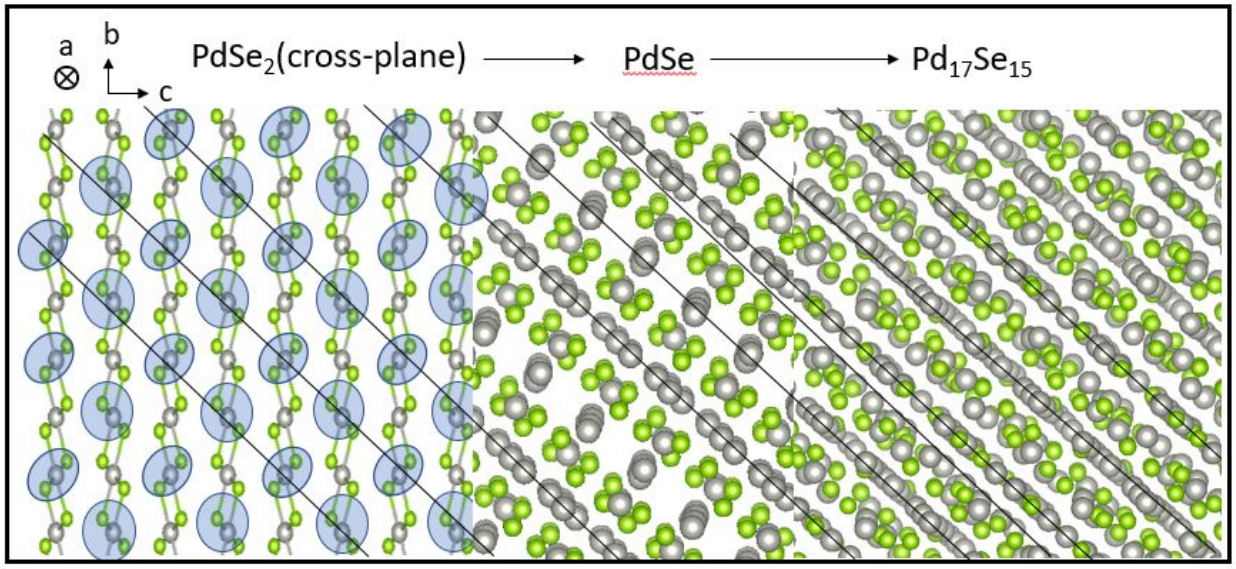

Figure S8. The phase transition reaction surface at the $PdSe_2$/PdSe/$Pd_{17}Se_{15}$ heterojunction.

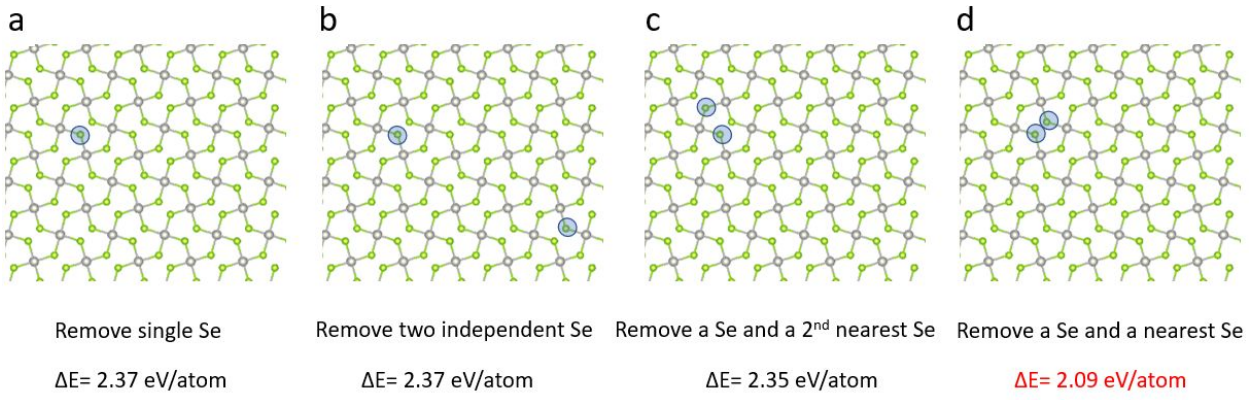

Figure S9. The energy needed for the removal of 1 and 2 Se atoms in a $PdSe_2$ layer. It is seen that the removal of a Se and its nearest Se, as shown in (d), is the most favorable.

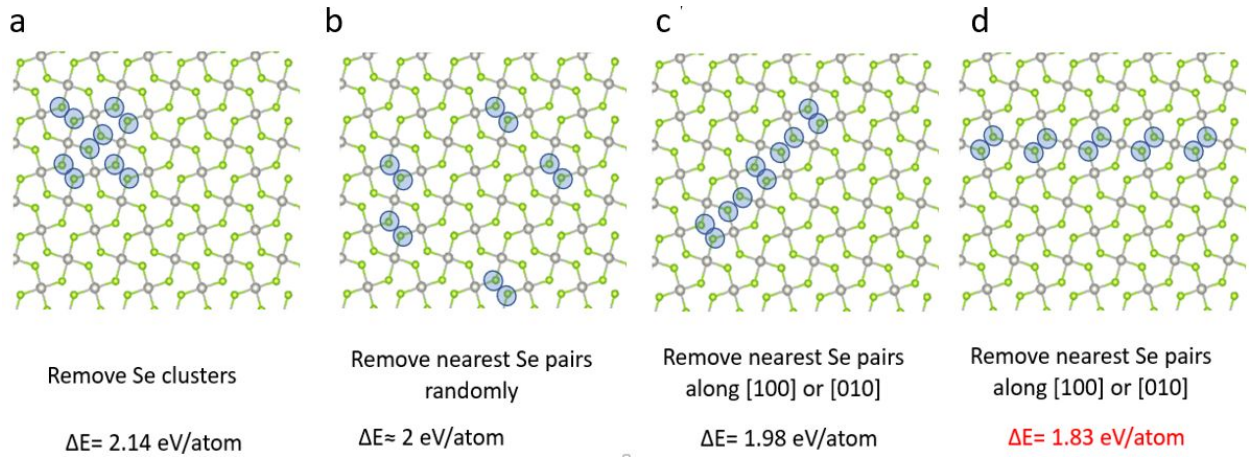

Figure S10. The energy needed for the removal more Se atoms in a $PdSe_2$ layer. It is seen that the removal of a Se along [100] or [010], as shown in (a), is the most favorable.

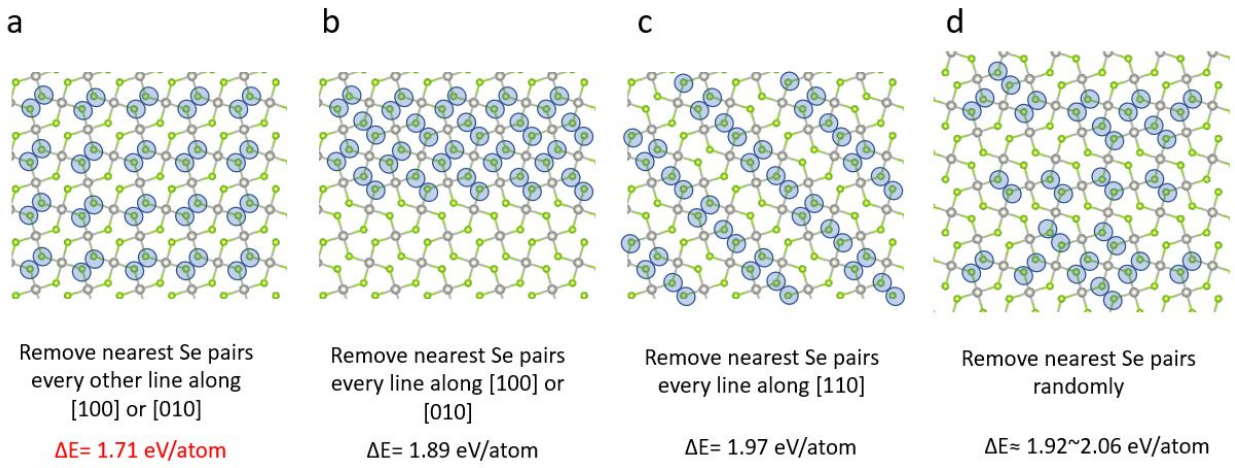

Figure S11. The energy needed for the removal half of the total Se atoms in a $PdSe_2$ layer. It is seen that the removal of Se nearest pairs every other line along [100] or [010], as shown in (a), is the most favorable.

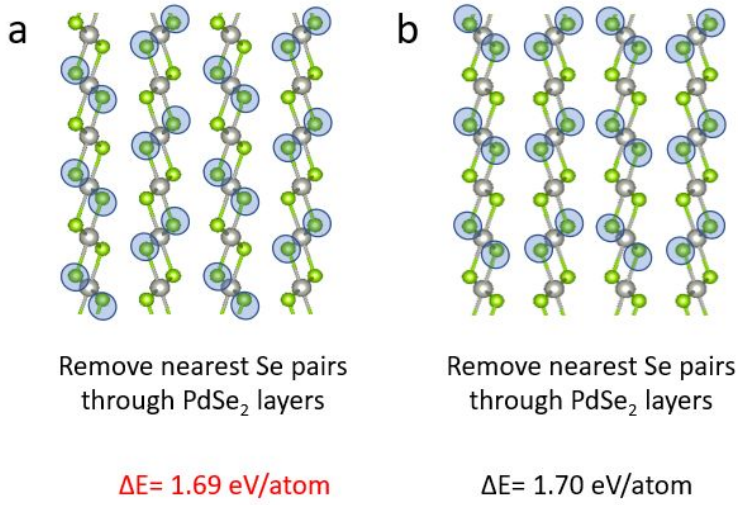

Figure S12. The energy needed for the removal half of the total Se atoms in a $PdSe_2$ layer. It is seen that the removal of Se nearest pairs every other line along [100] or [010], as shown in (a), is the most favorable.

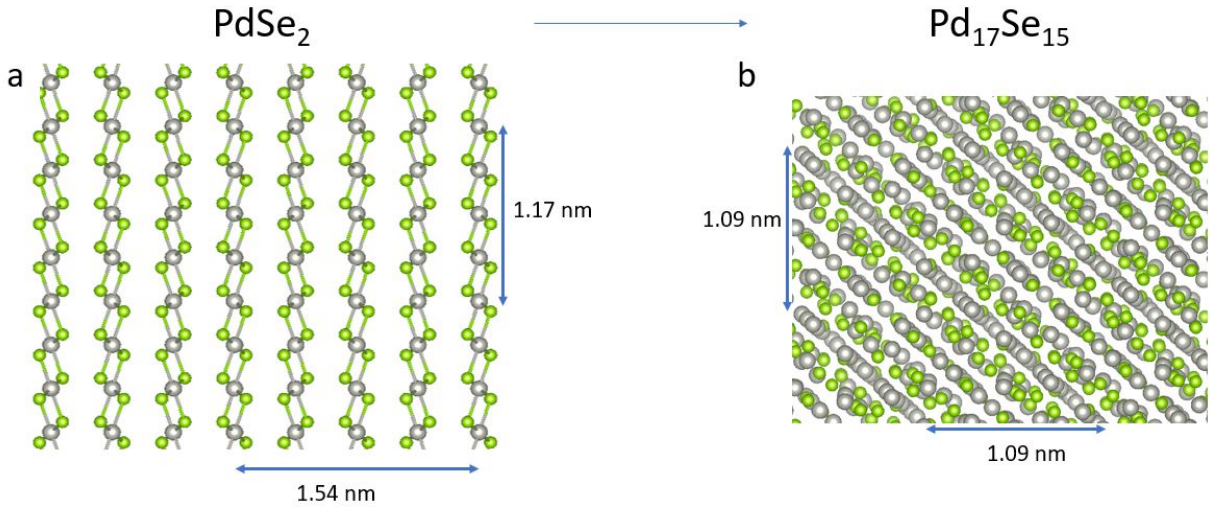

Figure S13. Theoretical dimensional shrinkage from $PdSe_2$ to $Pd_{17}Se_{15}$. The orientations of (a) and (b) are consistent with the transformation process in experiment. The thickness shrinks by 33%, and the in-plane dimension shrinks by 10%.

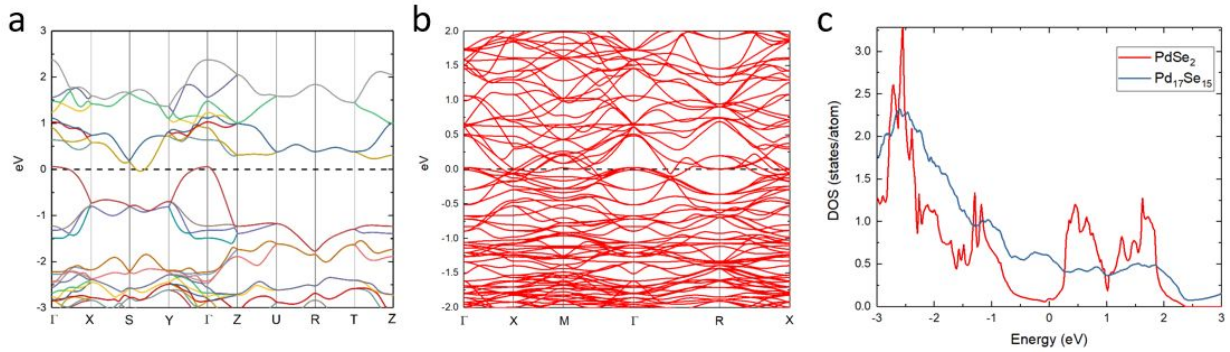

Figure S14. (a-b) Band structures of $PdSe_2$ and $Pd_{17}Se_{15}$ respectively, calculated from DFT. The Fermi level is at E=0. (c) Electron density of states for $PdSe_2$ and $Pd_{17}Se_{15}$. The Fermi level is at E=0.

4. Field-effect Transistor (FET) Device Characterization

A. Device fabrication, patterning, and measurement

Electron beam lithography (FEI DB-FIB with Raith pattern software) was used for device patterning. For samples with phase-patterned contacts, exposed areas were plasma treated. The metal contacts for the flakes, 5 nm of Ti followed by 30 nm Au, were deposited in vacuum using an electron beam evaporator. The FET device measurements were conducted in a cryo-enabled probe station using a Keithley 4200 semiconductor analyzer in a two-terminal configuration. The field effect mobility was extracted from the linear region of the device transfer characteristics using the equation, $\mu = \frac{L}{WC_{ox}}(\frac{\Delta I_{ds}}{\Delta V_g})$, where L is the channel length, W is the channel width, and $C_{ox} = 1.19 \times 10^{-4} F/m^2$ is the capacitance between the channel and the back gate per unit area, taken as $C_{ox} = \frac{\varepsilon_0 \varepsilon_r}{d_{ox}}$, where $\varepsilon_0 = 8.85 \times 10^{-12} F/m$, $\varepsilon_r = 3.9$ and d_{ox} = 280 nm.

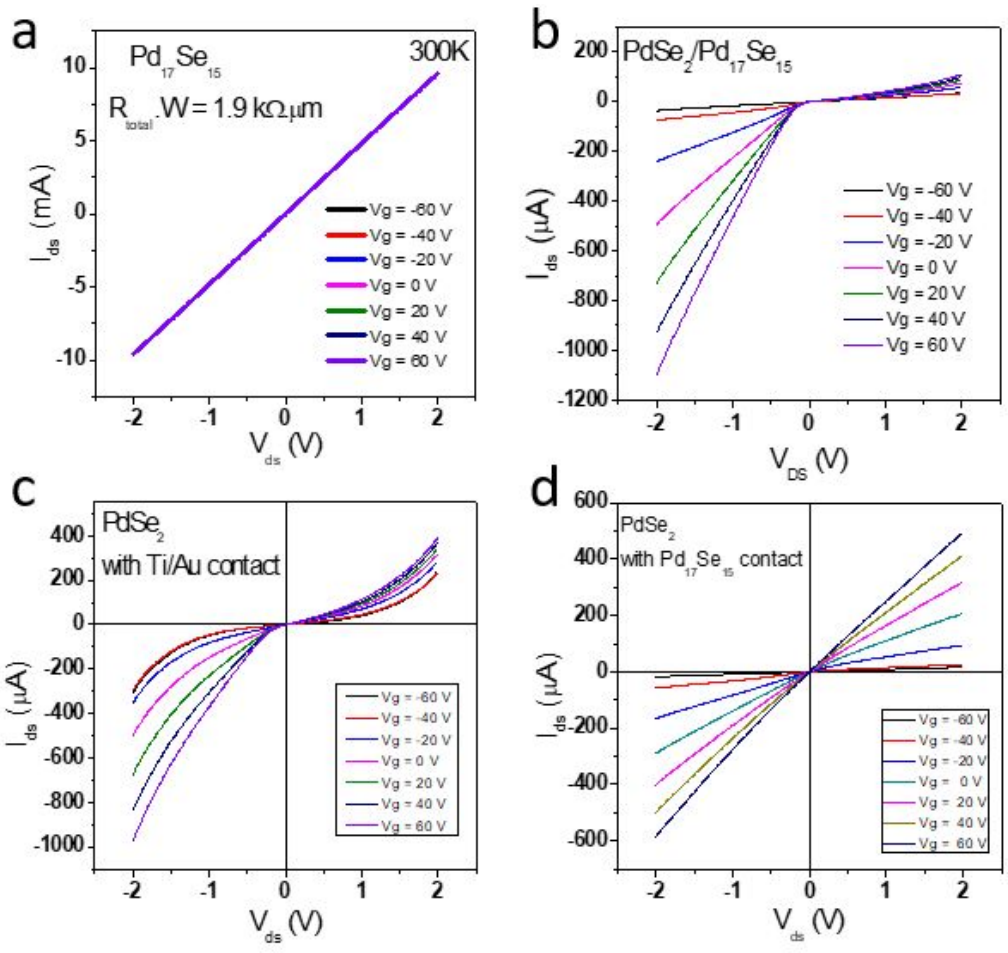

Figure S15. Typical output curves obtained for (a) $Pd_{17}Se_{15}$ showing no gate dependence, (b) $PdSe_2/Pd_{17}Se_{15}$ Schottky-junction showing rectifying behavior, (c) $PdSe_2$ with traditional Ti/Au contacts with non-linear I-V characteristics, and (d) $PdSe_2$ $Pd_{17}Se_{15}$ contacts with linear I-V characteristics.

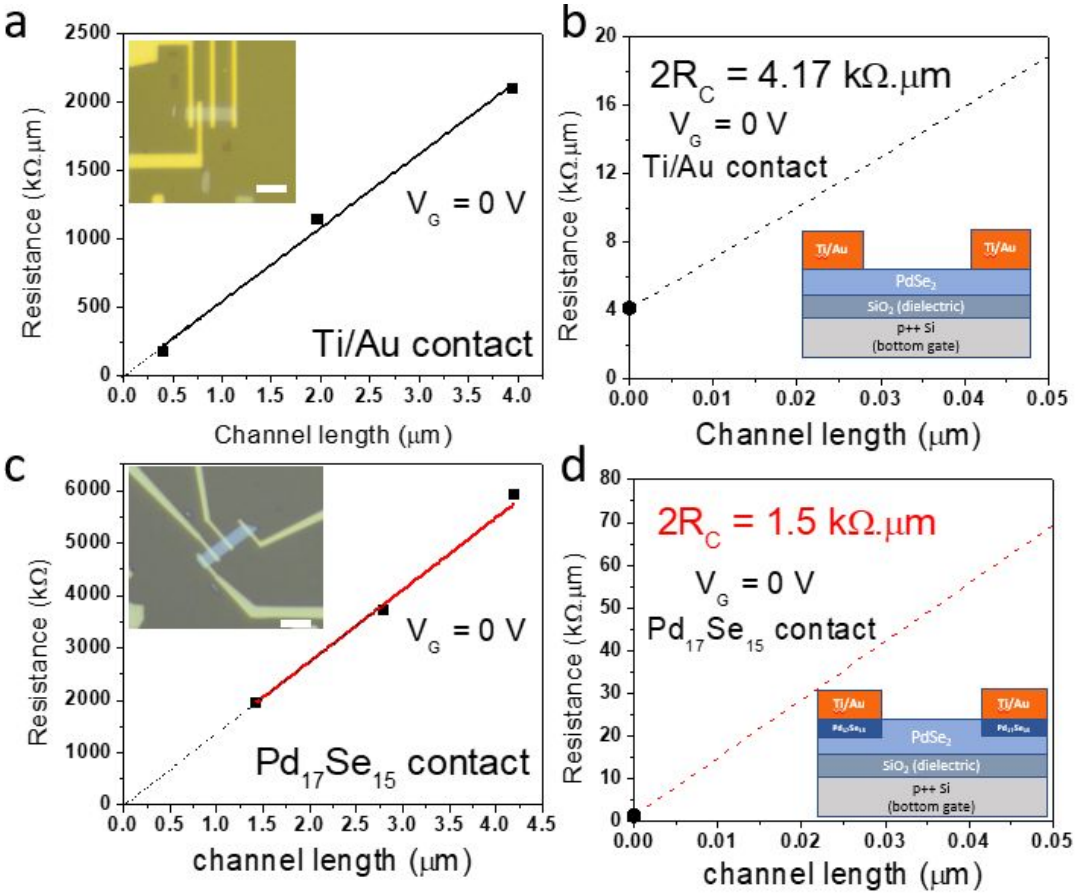

Figure S16. Transfer-length method (TLM) to obtain the contact resistance of $PdSe_2$ for Ti/Au deposited directly on the $PdSe_2$ (a,b) and for $PdSe_2$ device with seamless $Pd_{17}Se_{15}$ contact (c,d). The y-axis intercept of the resistances at different channel lengths yields contact resistances ($2R_c$) of 4.17 kΩ.μm for Ti/Au contacts (b) and 1.5 kΩ. μm for $Pd_{17}Se_{15}$ contacts (d) at zero gate bias. Optical microscope images and device schematics are also shown as insets. Scale bars in device optical images are 5 μm.

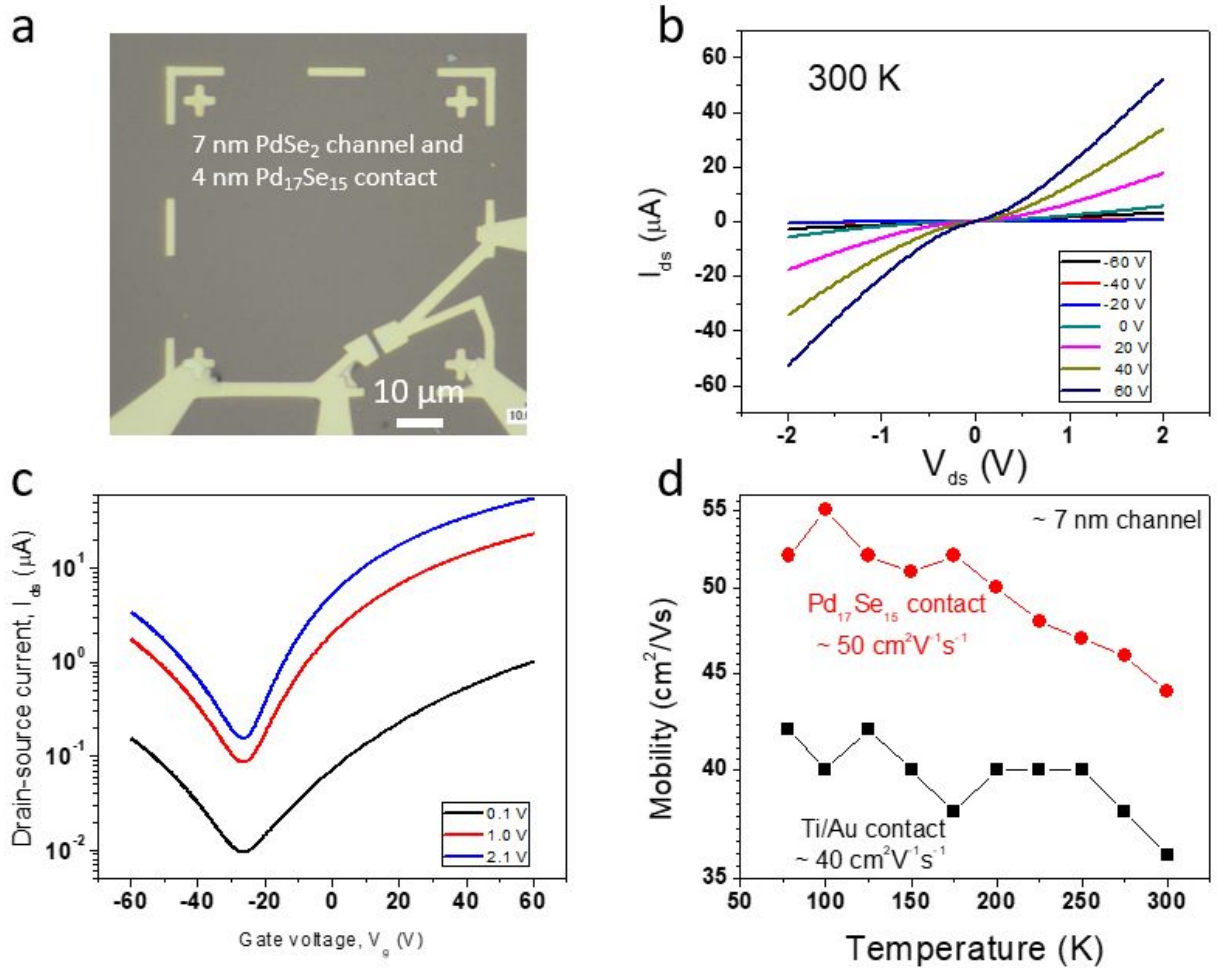

Figure S17. Device performance of thin $PdSe_2$ device with channel thickness of ~7 nm. (a) Optical micrograph (b) I_{ds}-V_{ds} output characteristics at different gate voltages. (c) Transfer characteristics showing predominantly n-type characteristics at different drain voltages measured at room temperature. (d) Plot of mobility at different temperatures comparing $PdSe_2$ device with $Pd_{17}Se_{15}$ contacts and traditional Ti/Au contacts.

B. Schottky-barrier height calculation

Using a two-terminal field-effect transistor (FET) configuration, the electrical properties of the new phase was studied. $Pd_{17}Se_{15}$ displayed a metallic behavior with no gate dependence with total resistivity of ~1.9 kΩ.µm as shown in Fig. S15 (a). This is in agreement with previous

studies conducted on the thin film and nanotube forms of $Pd_{17}Se_{15}$.[7,8] To understand the origin of the improvement in device performance, temperature-dependence electrical measurements were carried out to calculate the Schottky barrier at the $Pd_{17}Se_{15}$-$PdSe_2$ compared to the traditional metal-$PdSe_2$ interfaces. Fig. S18 (b) shows I_{ds}-V_{ds} plots at different temperatures from 75K – 300K for zero gate voltage while Fig. S18 (c) shows the corresponding log(I_{ds}) vs 1000/T plot at different voltage bias. The current-density of thermionic emission through a metal-semiconductor contact is

$$I_{DS} = AT^{3/2}\exp\left[-\frac{q}{k_B T}\left(\emptyset_B - \frac{V_{DS}}{n}\right)\right] \ldots \qquad \ldots\ldots\ldots(S1)$$

where A is the Richardson constant, V_{DS} is the applied voltage bias, T is the temperature, and k_B is the Boltzmann's constant.

The plot of the slope from the linear-regions of Fig. S18 (c) is shown in the main text (see Figure 4e), where Schottky barriers heights have been extracted as y-axis intercept. Schottky barrier height Φ_B, value from device with $Pd_{17}Se_{15}$ contacts ~3.26 meV is far less than ~96.20 meV obtained when traditional Ti/Au contacts used. This shows that the improvement in the device performance was as a result of the reduction in Schottky barrier height. Near-zero Schottky barrier heights are desired in electronic devices to facilitate a faster collection of charge carriers. For statistical purposes, several devices were fabricated with different thicknesses, with the Schottky barrier obtained shown in Table S5. These near-zero values show the presence of ohmic contacts, which is much lower than room temperature activation energy for carrier injection. The ability and ease to achieve ohmic contacts with the use of phase-transformed $Pd_{17}Se_{15}$ for $PdSe_2$, is promising for the electronic industry to achieve high-performance electronics.

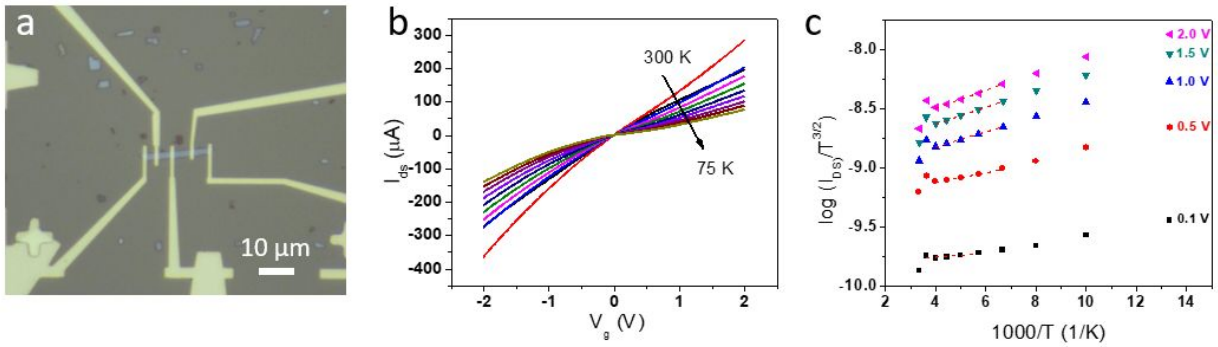

Figure S18. Transfer-length method (TLM). Typical optical image with electrodes creating different channel lengths on one device. (b) Temperature-dependent transfer characteristics. (c) The log(I_{ds}) versus 1/T curves at different drain bias.

Table S5. Comparison of the Schottky barrier heights at the heterointerface of metal-$PdSe_2$.

	$PdSe_2$ channel with $Pd_{17}Se_{15}$ contact	$PdSe_2$ channel with Ti/Au contact
Schottky barrier height (Φ_B) **Thickness of channel/contact**	3.52 meV 7 nm/4 nm	87.70 meV 5 nm/Ti (5 nm) Au (30 nm)
	5.81 meV 7 nm/4 nm	
	3.26 meV 55 nm/30 nm	96.20 meV 23 nm/Ti (5 nm) Au (30 nm)
	-1.85 meV 55 nm/30 nm	

Table S6. Comparison between two different contacts by our method and other reported methods

	$Pd_{17}Se_{15}$ contact/ Au contact	1T'$MoTe_2$ contact/ Au contact [9]	1T' $MoTe_2$ contact/ Au contact [10]	1T MoS_2 contact/ Au contact [11]
Contact resistance (kΩ·μm)	~0.75/~2.08	~14/N	~0.1/~1	~0.24/~1.1
Mobility ($cm^2V^{-1}s^{-1}$)	~170/~8	~16.2/~4.0	~50/~1	~46/~19
Schottky barrier height (meV)	~96/~3	~22/~150	~10/~200	N

References

1 Oyedele, A. D. *et al.* $PdSe_2$: Pentagonal Two-Dimensional Layers with High Air Stability for Electronics. *J Am Chem Soc* **139**, 14090-14097 (2017).

2 Puretzky, A. A. *et al.* Anomalous interlayer vibrations in strongly coupled layered $PdSe_2$. *2d Mater* **5**, 035016 (2018).

3 Geller, S. Crystal Structure of $Pd_{17}se_{15}$. *Acta Crystallogr* **15**, 713 (1962).

4 Sutter, E. *et al.* Electron-Beam Induced Transformations of Layered Tin Dichalcogenides. *Nano Lett* **16**, 4410-4416 (2016).

5 Sun, J. F., Shi, H. L., Siegrist, T. & Singh, D. J. Electronic, transport, and optical properties of bulk and mono-layer $PdSe_2$. *Appl Phys Lett* **107**, 153902 (2015).

6 Soulard, C. *et al.* Experimental and theoretical investigation on the relative stability of the PdS2- and pyrite-type structures of $PdSe_2$. *Inorg Chem* **43**, 1943-1949 (2004).

7 Kukunuri, S., Austeria, P. M. & Sampath, S. Electrically conducting palladium selenide (Pd_4Se, $Pd_{17}Se_{15}$, Pd_7Se_4) phases: synthesis and activity towards hydrogen evolution reaction. *Chemical Communications* **52**, 206-209 (2016).

8 Kukunuri, S., Karthick, S. & Sampath, S. Robust, metallic $Pd_{17}Se_{15}$ and Pd_7Se_4 phases from a single source precursor and their use as counter electrodes in dye sensitized solar cells. *Journal of Materials Chemistry A* **3**, 17144-17153 (2015).

9 Sung, J. H. *et al.* Coplanar semiconductor-metal circuitry defined on few-layer $MoTe_2$ via polymorphic heteroepitaxy. *Nat Nanotechnol* **12**, 1064 (2017).

10 Cho, S. *et al.* Phase patterning for ohmic homojunction contact in $MoTe_2$. *Science* **349**, 625-628 (2015).

11 Kappera, R. *et al.* Phase-engineered low-resistance contacts for ultrathin MoS_2 transistors. *Nat Mater* **13**, 1128-1134 (2014).